Studies of the CMS Level 1 Trigger and Tracker Upgrade

Yi Liu

A dissertation submitted to the University of Bristol in accordance with the requirements for award of the degree of Masters by Research in the School of Physics.

School of Physics

University of Bristol

April 2019

Abstract

The Large Hadron Collider (LHC) is the world's largest and most powerful particle accelerator. It found the Higgs particle in 2012. In order to fully exploit the potential of the LHC, it is planned to upgrade to the High-Luminosity LHC (HL-LHC), reaching a peak luminosity of $5 - 7.5 \times 10^{34}$ cm^{-2}s^{-1}. The Compact Muon Solenoid (CMS) detector, as one of four detectors at the LHC, will be upgraded to operate at the HL-LHC. One of the most important aspects of this upgrade will be the addition of track information in the Level-1 trigger system.

In this thesis, we will present the concept of the CMS tracker and trigger system upgrade including the limitations of the current trigger system. The implementation of the track trigger via a Hough transform will be discussed. Simulations of the track trigger system show that more than 90% of tracking particles can be reconstructed over the full acceptance. We also discuss the relationship between the tracker layout and the number of reconstructed tracks. The performance of the track trigger for tracks generated at different positions in the z-direction is shown. By changing the cell size of the Hough transform, the performance of the track trigger system changes. The best performance is obtained with a granularity of 32x64 cells per sector. The effect in the performance of the Hough transform due to dense track environments will be discussed last.

Dedication

To my family.

Acknowledgements

First of all, I would like to thank Professor Joel Goldstein, my supervisor, for introducing me to the fantastic world of particle physics, continually guiding me and giving me confidence and knowledge on this road. His careful guidance of my thesis improved my understanding of academic writing.

Thanks to Dr Emyr Clement and Dr Tai Sakuma. They supported me a lot and always helped me.

Declaration

I declare that the work in this dissertation was carried out in accordance with the requirements of the University's Regulations and Code of Practice for Research Degree Programmes and that it has not been submitted for any other academic award. Except where indicated by specific reference in the text, the work is the candidate's own work. Work done in collaboration with, or with the assistance of, others, is indicated as such. Any views expressed in the dissertation are those of the author.

Contents

1 Introduction **1**

1.1 Particle Physics and the Standard Model 1

1.2 Large Hadron Collider 5

1.3 High Luminosity LHC 8

1.4 CMS detector 9

1.5 The CMS trigger system 12

1.6 Production of jets 13

1.7 Simulation Platform 14

2 The CMS Phase 2 Upgrade **15**

2.1 The CMS L1 trigger upgrade 15

2.2 The CMS tracker upgrade 18

2.3 The Level-1 track trigger 21

2.4 Hough transform 23

3 Performance of the Track Trigger **27**

3.1 Analysis Method 27

3.2 Track trigger performance dependence on p_T 28

3.3 Track trigger performance as function of angle 31

3.3.1 Track trigger performance as function of angle for different z origins 33

4 Track Trigger Efficiency In Dense Tracking Environments **37**

5 Effect of the Cell Size in the Hough Transform 43

6 Conclusion 47

Bibliography 49

Chapter 1

Introduction

1.1 Particle Physics and the Standard Model

Particle physics is an important branch of modern physics which focuses on researching what the elementary constituents of the world are. In the current understanding, a particle is an excitation of a quantum field. The dominant theory explaining the origin of particles and their interactions is called the Standard Model of particle physics (SM). The SM describes three generations of matter (quarks and leptons), four gauge bosons and one Higgs boson, shown in Figure 1.1.

The six quarks and six leptons, which are the elementary constituents of matter, are fermions (a fermion is a particle that follows Fermi–Dirac statistics, while bosons obey Bose–Einstein statistics). The up quark and the down quark form the first generation, then the charm quark and strange quark. The third generation is the bottom quark and top quark. The six leptons are arranged in a similar fashion to the quarks. The electron and electron neutrino are in the first generation, followed by the muon and the muon neutrino, and the tau and the tau neutrino. The electron, the muon and the tau have an electric charge while the neutrinos are neutral and have little mass. The first generation particles are lighter and more stable than their corresponding particles in the second and third generations. All stable matter in the universe is made from particles that belong to the first generation; any heavier particles quickly decay to more stable ones.

There are four known fundamental forces working in the universe: the electromagnetic force, the strong force, the weak force and the gravitational force. They have different ranges and strengths. Gravity and the electromagnetic force have an infinite range and the strength of the latter is many times larger than gravity, which is the weakest among the four. The strong force and weak force have a subatomic-level range. The strong force is the strongest of all of the four fundamental interactions, while the weak force, as it name suggests, appears to be the weakest except for gravity. Three of the forces (electromagnetic, strong and weak) are described in the SM by quantum field theory (QFT) and their interactions are mediated by gauge bosons. Specifically, the photon is the gauge boson for the electromagnetic interaction, the W and Z boson are for the weak interaction and eight gluons is for the strong interaction. The gravitational force is described by general relativity (GR) which is not included in the SM.

There is one Higgs boson, a neutral, unstable elementary particle with spin 0. The Higgs boson is produced by the quantum excitation of the Higgs field, which is regarded as giving mass to all fundamental particles by the Higgs mechanism, the remarkable offspring of the marriage of local gauge invariance and spontaneous symmetry-breaking [1]. Specifically, the spontaneous symmetry-breaking gives mass to W and Z bosons. Fermions also gain mass by some kind of Yukawa coupling between the fermion fields and the Higgs field [2].

The SM can describe three of the four fundamental forces (electromagnetic, weak and strong interaction), but not gravity. The effect of gravity is so weak that it is negligible in the microscopic scale, so the SM still works well to describe the particle world.

The SM also has some unexplained features, such as the hierarchy problem and dark matter. The hierarchy problem is that some fundamental physical parameters, such as coupling constants, have a vast difference between the value measured in experiment and expected from a fundamental theory. Typically, the effective value is related to the fundamental value by a correction method known as renormalisation.

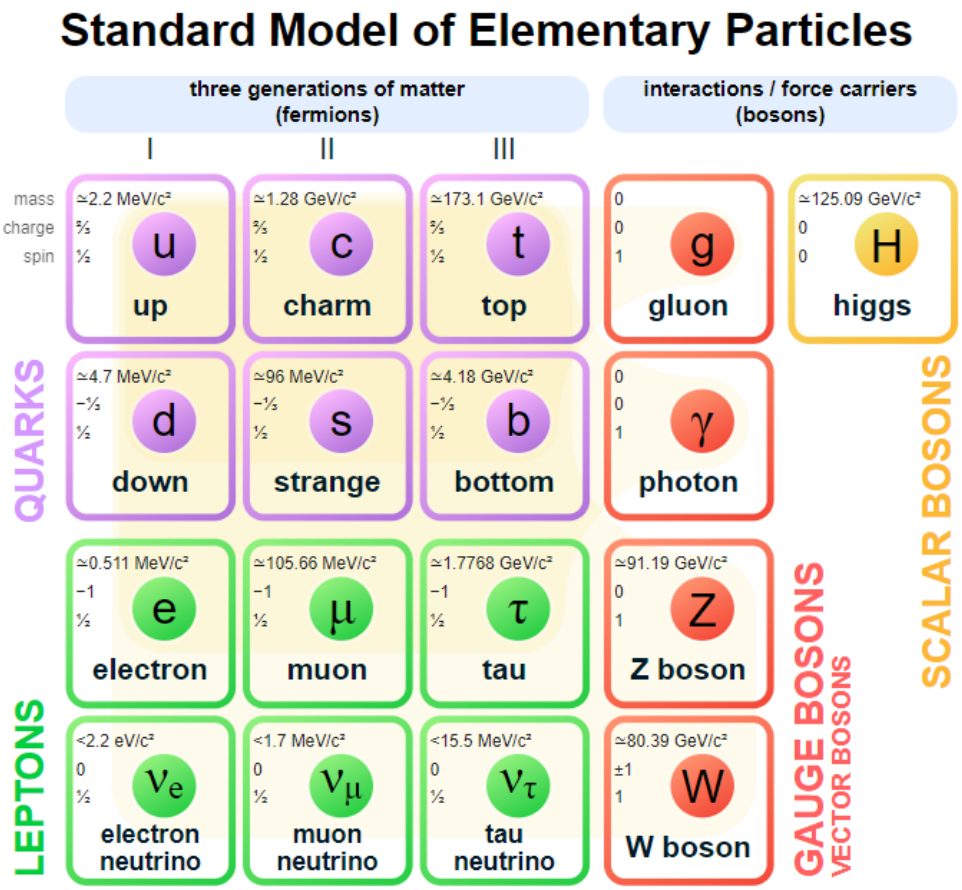

Figure 1.1: The standard model of elementary particles[3]

But in some cases, the renormalisation is unnatural. For example, one of the most important hierarchy problems is why the Higgs boson (125 GeV) is much lighter than the Planck mass (10^{19} GeV). The large quantum contribution shown in the top part of Figure 1.2 requires almost perfect cancellation with the fundamental value resulting in the observed mass of 125 GeV [4]. This cancellation mechanism is still pursued by particle physicists.

Dark matter is a hypothetical form of matter that does not interact with the electromagnetic force, such as light, and is thus invisible in the entire electromagnetic spectrum, making it extremely hard to spot. So far, dark matter can be detected only by its gravitational effects. It is thought that dark matter accounts for 27% of the whole universe which is five times larger than visible matter. The rest of the universe is dark energy. Some theories predict that dark matter consists of light particles (less than 1 TeV) and can be produced in particle colliders and it

escapes through detectors unnoticed. However, the dark matter particle would carry energy and momentum, which leads physicists to try to find "missing" energy and momentum after a collision. So far, dark matter has not been detected. Many models predict weakly-interacting massive particles (WIMPs) which could be produced at colliders.[5].

One of the theoretical solutions to the hierarchy problem and dark matter is Supersymmetry (SUSY), which proposes a relationship between bosons and fermions. SUSY predicts that each of the particles in the SM has a partner with a half unit difference of spin, shown in Figure 1.3. As bosons and fermions have opposite sign loop corrections, shown in figure 1.2, SUSY makes the cancellation between the top quark and its superpartner ($\tilde{t}$) natural. The lightest SUSY particle is colorless, neutral, and stable, making it an attractive candidate for dark matter[1].

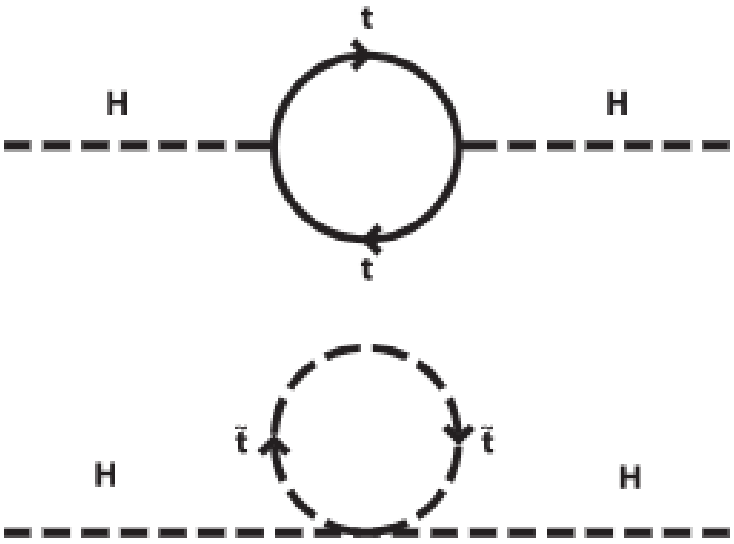

Figure 1.2: The tadpole Feynman diagrams showing the cancellation of the Higgs boson mass renormalization between fermionic top quark loop and stop quark loop

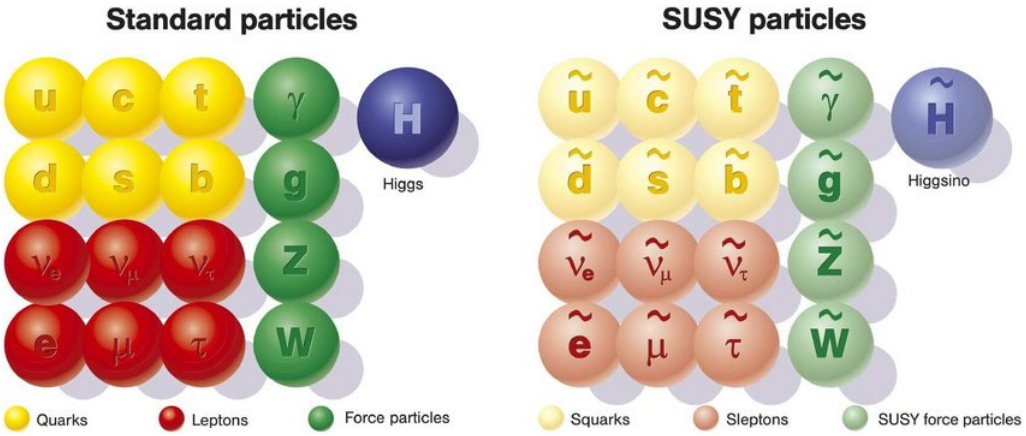

Figure 1.3: Standard model particles and corresponding superpartners.

1.2 Large Hadron Collider

The Large Hadron Collider (LHC) is the world's largest and most powerful particle accelerator. The LHC can accelerate protons and heavy ions such as lead. In order to achieve the highest energy in the center of mass frame, colliding beams are better than a moving particle on a fixed target. Thus, the LHC creates two opposite moving beams in two adjacent pipes to make collisions. Superconducting electromagnets produce a strong magnetic field in order to guide the particles [6].

Luminosity $\mathcal{L}$, an important parameter for the performance of a collider, is proportional to the number of collisions in a fixed time [7]. Luminosity is the ratio of the number of events produced N in a certain time t to the interaction cross-section σ. Increasing luminosity produces more collision data from the experiment, which gives the opportunity to observe rare effects.

$$\mathcal{L} = \frac{1}{\sigma}\frac{dN}{dt} \tag{1.1}$$

The LHC has delivered collisions of protons (pp), lead ions (PbPb) and protons with lead ions (pPb). There are four collision points in the LHC ring, and people have built a particle detector at each point: the CMS detector, the ATLAS detector, the ALICE detector and the LHCb detector, shown in Figure 1.4.

Both CMS and ATLAS are general-purpose detectors. They have a wide physics

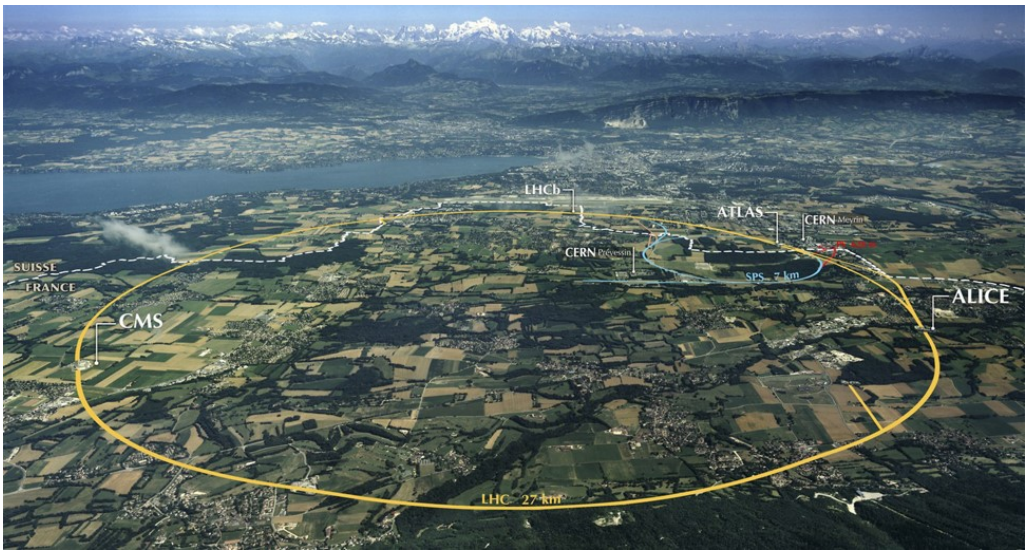

Figure 1.4: The LHC lies in a tunnel 27 kilometers in a circumference and as deep as 175 meters, on the France and Swiss border near Geneva.

research range: from studying the SM to searching for the particles that could make up dark matter. The differences between them are technical choices for detector and magnet-system design. The ALICE (A Large Ion Collider Experiment) is a heavy ion detector. It is designed to research quark-gluon plasma which is produced in strongly interacting matter at extreme energy densities. The LHCb (Large Hadron Collider beauty) detector is for studying bottom quarks in order to investigate the slight difference between matter and antimatter.

The LHC started operation in 2009. The running period from 2010 to 2012 is referred to as Run 1, with a centre-of-mass energy, $\sqrt{s}$, of 8 TeV. After a two-year shutdown, referred to as Long Shutdown 1 (LS1), Run 2 started in 2015 at $\sqrt{s} =$ 13 TeV and continued until the end of 2018. The plan of the LHC from 2015 is shown in Figure 1.5. Run 2 will be followed by the Long Shutdown 2 (LS2). Run 3 will start in 2021 and end in 2023, After that, the main upgrade for the high luminosity LHC (HL-LHC) will proceed in LS3, while some upgrades will be done in LS2, such as the upgrade of the LHC injector complex.

There have been many achievements from the four experiments. The Higgs boson was discovered in the mass region around 125 GeV by CMS and ATLAS in 2012 [9][10], shown in Figure 1.6. The measurement of the branching ratios of the rare

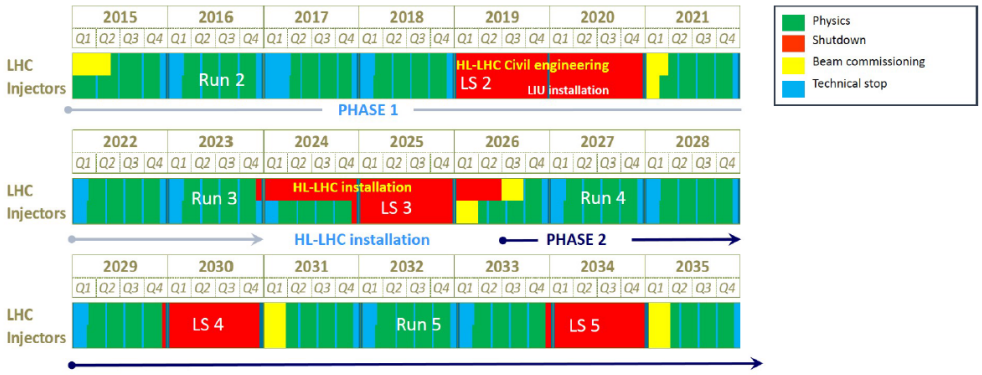

Figure 1.5: The overview of the plan of the LHC. Data taking phases are green (Run) and shutdown time is red, labelled LS. It also shows beam commissioning (yellow) and technical stop (blue) phases [8]

decays of the neutral B_s^0 and B^0 mesons to two muons was made by CMS, LHCb and ATLAS. Both measurements are statistically compatible with SM predictions and allow stringent constraints to be placed on theories beyond the SM [11], challenging the validity of various SUSY models.

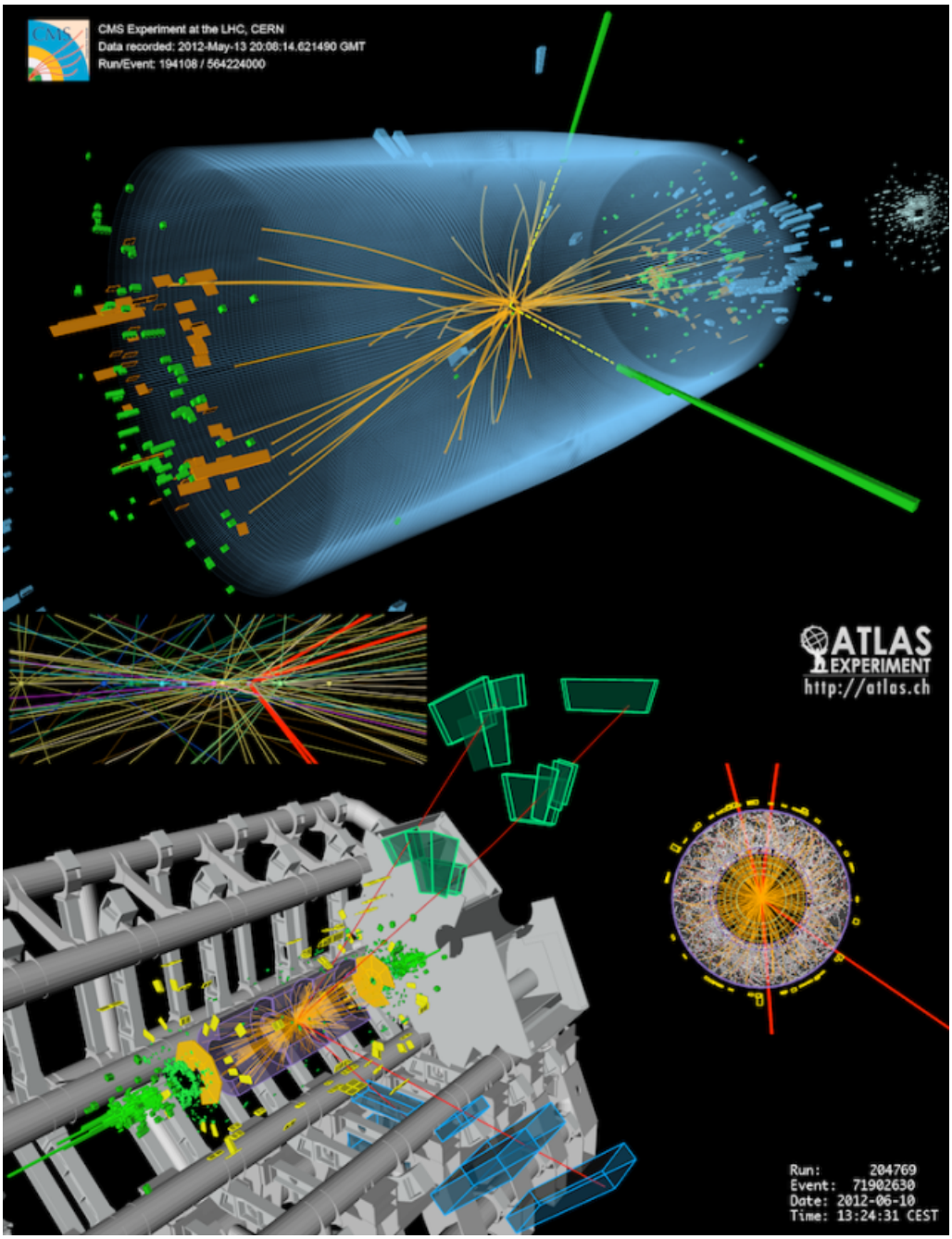

Figure 1.6: The production of Higgs bosons from proton-proton collisions. The upper event shows a decay into two photons (dashed yellow line) in the CMS experiment. The lower event shows a decay into four muons represented by red lines in the ATLAS experiment

1.3 High Luminosity LHC

In order to exploit the potential of the LHC, it is planned to increase the luminosity of the machine by an order of magnitude, which will take a 30 month shut down starting around 2024. After this period, the High-Luminosity LHC (HL-LHC) will

reach a peak luminosity of $5 - 7.5 \times 10^{34}$ cm^{-2}s^{-1}[12]. This corresponds to an environment of 140-200 proton-proton interactions, named pileup (PU), per LHC bunch crossing. The HL-LHC can produce 15 million Higgs bosons per year, compared to the 1.2 million produced from 2011-2012.

The HL-LHC can enhance the rate of rare events and provide the highest precision in investigating the SM and BSM. For example, the Higgs boson coupling is a crucial part of the SM. The HL-LHC will enhance the measurement precision for Higgs couplings in the CMS experiment, such as the coupling to muons. The self-coupling of the Higgs boson probes the Higgs field. However, the cross section of Higgs boson pair (HH) production is about 1000 times smaller than the cross section of single Higgs boson production. The Feynman diagram of HH production is shown in Figure 1.7 [13] . HL-LHC is expected to measure these rare production modes in the future [14].

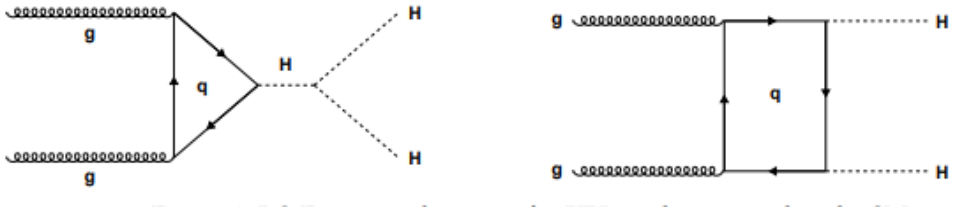

Figure 1.7: Leading-order Feynman diagrams for HH production, where q stands for quark, top and bottom quark dominate.

1.4 CMS detector

The Compact Muon Solenoid detector (CMS) is a large, general purpose particle detector located at one of the collision points of the LHC, From Figure 1.8 and Figure 1.9, it can be seen that the CMS detector is like a cylindrical onion with several layers with different functions.

The CMS experiment uses a right-hand coordinate system. The origin is at the collision point, the x-axis is in the LHC plane pointing to the centre of the LHC ring, the y-axis points up which is perpendicular to the LHC plane, the z-axis points along the anticlockwise beam direction. The azimuthal angle (ϕ) is measured from

the positive x-axis in the x-y plane and the polar angle (θ) is measured from the positive z-axis. The radius (r) represents the distance from the origin in the x-y plane and the definition of pseudorapidity is $\eta = -\ln\tan(\theta/2)$. Angular distance is defined as $\Delta R = \sqrt{\Delta\phi^2 + \Delta\eta^2}$.

The tracker system is the nearest sub-detector to the collision point. It can detect the trajectory of a charged particle when it passes through the layers of silicon sensors. Charged particles also are deflected in the magnetic field by the Lorentz force. The higher the momentum of the particle the less its trajectory bends. Thus by collecting hits in sensors, the tracker system can rebuild the trajectory and momentum of charged particles. Figure 1.10 shows the layout of one quarter of the tracker.

The electromagnetic calorimeter (ECAL) is the second nearest sub-detector from the collision point. It is made from crystals of lead tungstate. Charged particles release energy in the tungstate crystals and produce secondary particles and light. Photon-detectors can detect the photons emitted and calculate the energy by software. The hadron calorimeter (HCAL) measures the energy of hadrons such as protons, neutron, kaons and pions. It has the same working principle as the ECAL: hadrons hit the absorber material and produce secondary particles, which can be detected and the energy calculated. The superconducting solenoid is a 13 meters long and 6 meters diameter coil of niobium-titanium superconductor, and produces a magnetic field of 4 Tesla. This field bends the trajectories of charged particles, enhancing separation and allowing momentum measurements. The muon system is located in the external layers of the CMS detector as muons can pass through several metres in ordinary matter and cannot be stopped by the calorimeters. When a muon passes through the muon chamber, it knocks out electrons from the gas contained in the muon chamber and produces an electrical signal. In order to define the trajectory of muons, data from the tracker system and muon system can be combined.

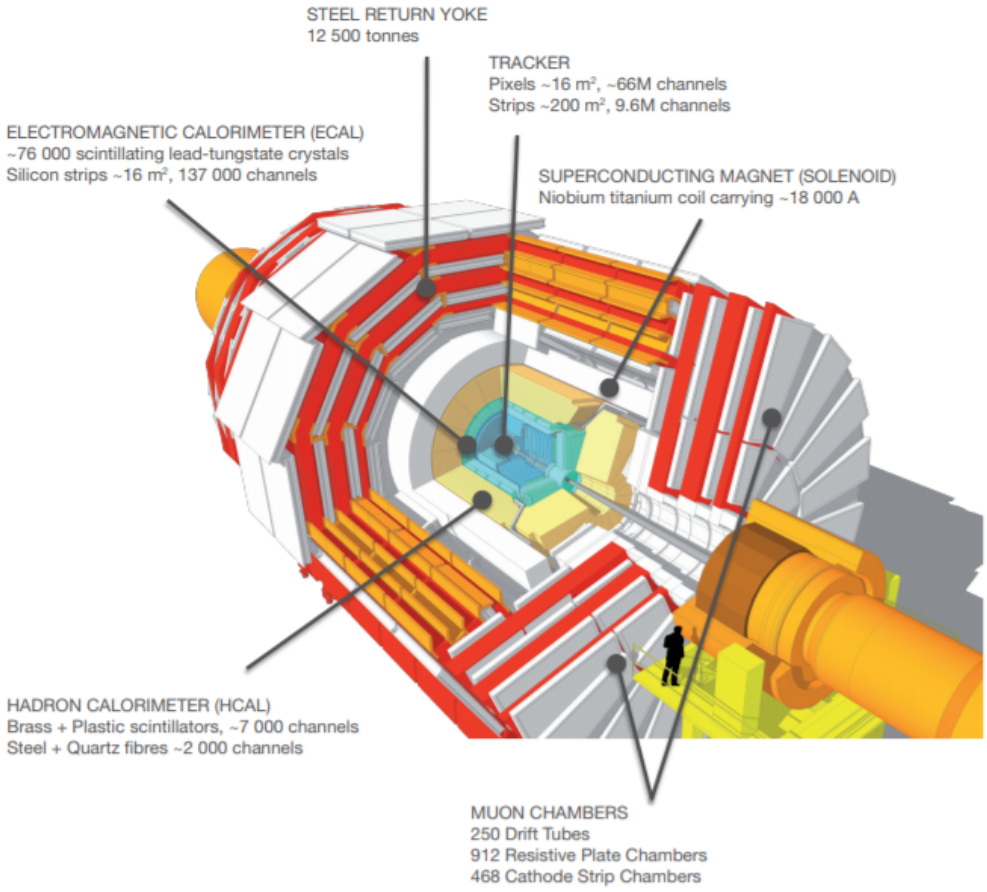

Figure 1.8: The CMS detector

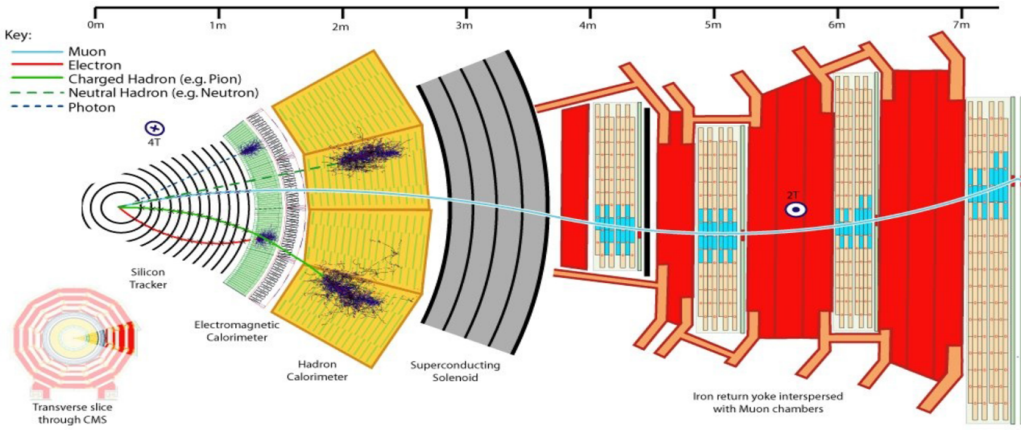

Figure 1.9: A segment of the CMS detector in transverse view. The blue line is a muon track, passing through the tracker and the calorimeter with a track. The red line represents an electron: it bends in the tracker and interacts in the ECAL. The trajectory of a charged hadron is represented by the solid green line. The dashed green line and dashed blue line are a neutral hadron and photon respectively.

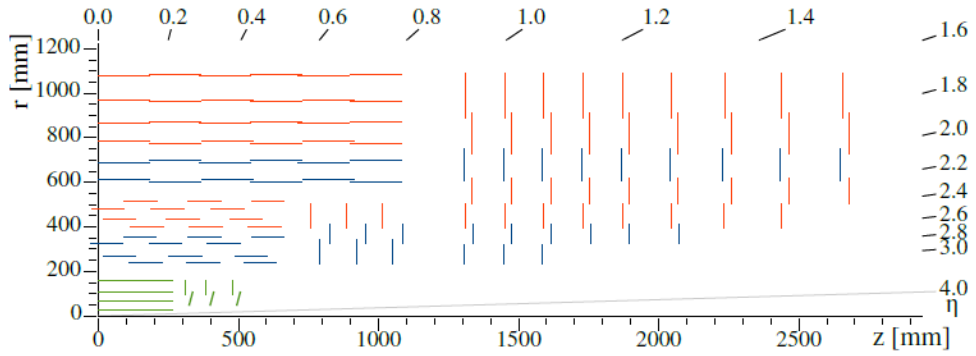

Figure 1.10: A quadrant of the CMS tracking system in the $r - z$ view. The green lines represent the pixel detector. Single-sided and double-sided strip modules (composed of two back-to-back silicon strip detectors with a stereo angle of 100 mrad) are shown as red and blue, respectively. The coverage of the system is up to a pseudorapidity of $|\eta| < 2.4$

1.5 The CMS trigger system

The LHC delivers 40 Mhz proton-proton collisions, which produces a huge amount of data. It is impossible to store all the data so a trigger system is needed. The trigger system does a pre-selection to find "interesting" collisions and discards the rest of the data (99.99999%). At present, the CMS trigger system has two levels: the Level 1 trigger (L1 trigger) and the High-Level Trigger (HLT). The L1 trigger has hardware processors that get data from the calorimeter and muon system, and which generates a trigger accept signal within 3 μs and reaches a maximum output rate of 100 kHz. The HLT decreases the data rate further, reaching about 1 kHz by using software [15].

An overview of the L1 trigger system is shown in Figure 1.11. Trigger primitives are generated from the forward hadron calorimeter (HF), HCAL, ECAL and the muon detector (resistive-plate chambers (RPC), cathode strip chambers (CSC) and drift tubes (DT)). Before being combined in the global trigger (GT), both the trigger primitives from the calorimeter and those from the muon detector pass through several steps [16].

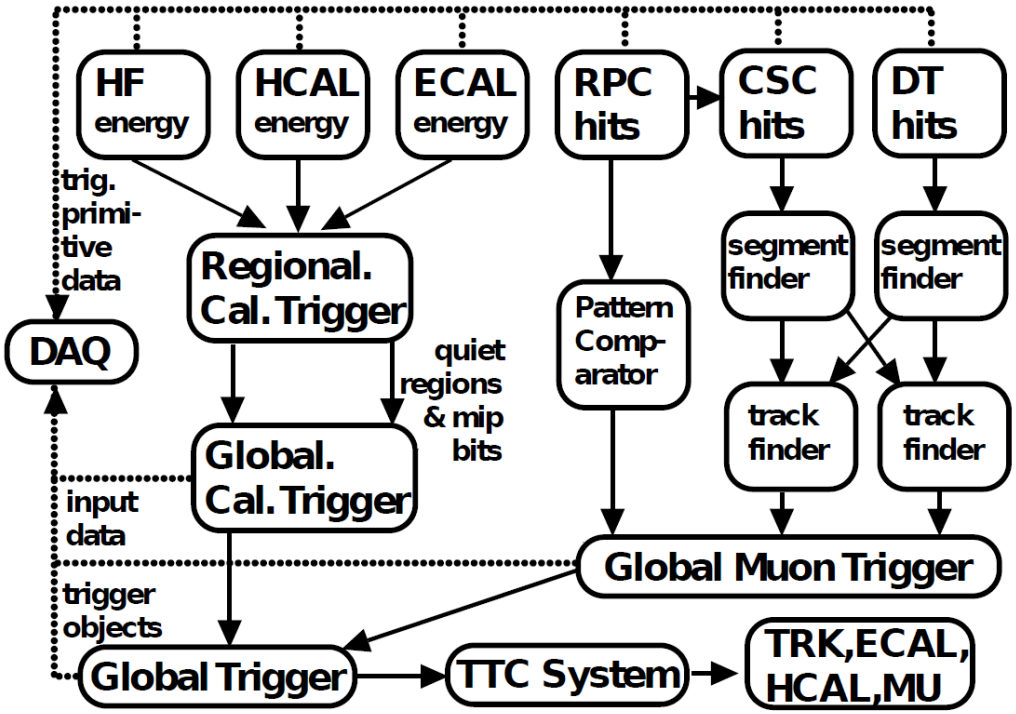

Figure 1.11: A schematic of the CMS L1 trigger system. The trigger primitives from HF, HCAL and ECAL are combined firstly in the regional calorimeter trigger (RCT) and then transfered to the global calorimeter trigger (GCT). Energy deposits (hits) from the RPC, CSC and DT are processed by pattern comparator or segment-tracker finder and sent to the global muon trigger (GMT). The global trigger (GT) combines information from the GCT and GMT to make the final trigger decision. The decision information flows to the tracker (TRK), ECAL, HCAL and muon system (MU) through the tigger, timing and control (TTC) system. The data acquisition system (DAQ) reads data from subsystems for offline storage.

1.6 Production of jets

A jet is a quantum chromodynamics (QCD) phenomenon in high-energy processes. Quarks and gluons have a net colour charge. Due to colour-confinement, individual quarks and gluons cannot be observed in nature. They will combine to form colour-neutral hadrons, a process called hadronization which leads to a collimated spray of hadrons called a jet as shown in Figure 1.12.

Jets play an important role in collision analysis. In the CMS experiment, a jet of particles leaves signals in sub-detectors, such as TRK, ECAL and HCAL. We combine these signals to reconstruct jets via a jet algorithm. By measuring the energy of particles in a jet, the energy and particle properties before hadronization

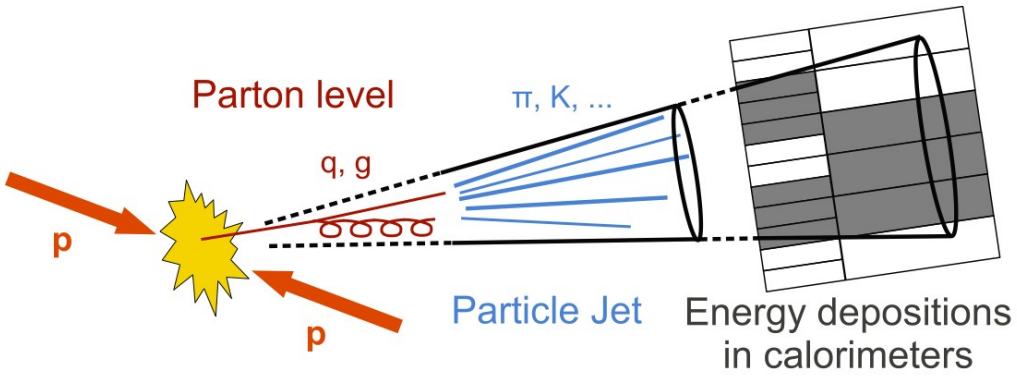

Figure 1.12: Sketch of pp-collision and resulting collimated spray of particles, a jet.

can be estimated. For example, three jet events are strong evidence for the existence of the gluon, observed first in DESY in 1979 [17].

1.7 Simulation Platform

The platform for simulation and data analysis in CMS is CMSSW. The CMSSW is a collection of software used to perform analysis using collision data and MC data samples. It includes a framework, an Event Data Model (EDM) and functions including the simulation, calibration and alignment, and reconstruction. The framework and EDM aim to optimise the development of reconstruction and analysis software.

The EDM is centered around the concept of the event. The raw and reconstructed data is stored in a C++ object, called an event. The framework of CMSSW uses a "software bus" model which means the data passes to a series of modules.

The CMSSW event processing model consists of one executable, called cmsRun, which includes many plug-in modules managed by the framework which are loaded at runtime. The modules contain all the event processing code, such as calibration, reconstruction algorithms, etc. The cmsRun is configured by a configuration file. The configuration file defines which modules are loaded, in which order they are run, and with which configurable parameters they are run [18]. The version used in this article is CMSSW9_3_4.

Chapter 2

The CMS Phase 2 Upgrade

The CMS detector plans to upgrade during LS3 to prepare for the increase in luminosity provided by the HL-LHC. This upgrade is referred to as the CMS Phase-2 Upgrade. The increased radiation requires a higher radiation hardness. The larger pile-up and density of particles requires that the detector has a higher resolution. The trigger system also needs to be improved in order to keep the trigger rate at an acceptable level.

2.1 The CMS L1 trigger upgrade

In the HL-LHC, the key mission of the CMS experiment includes precise measurement of particles' properties, especially for the newly found Higgs boson, and the search for clues for new physics. High luminosity expands the mass range we can reach and enhances the number of rare events. Therefore, maintaining the overall physics acceptance (sensitivity to process of interest) is an important task for the Phase-2 Upgrade. It requires the CMS experiment to retain the capability to trigger events reliably in low mass-range physics processes (e.g. Higgs production at 125 GeV), and to make precision measurements of leptons, photons and jets. In order to achieve these, the trigger system needs upgrading during LS3.

It is challenging for the L1 trigger system to select interesting physics events at high luminosity. This is not only due to the increasing interaction rate, but also the

selections algorithms become inefficient in high pile-up conditions. The simplest way to satisfy the high rate in HL-LHC with a limited bandwidth, is for the thresholds for object selection to increase. Raising thresholds leads to the loss of physics sensitivity, for example in the decay of the Higgs boson to two Z bosons, which in turn decay to charged leptons (e, μ). The Feynman diagram is shown in Figure 2.1. The leptons can be measured precisely and the decay can be completely reconstructed, which relies on the identification and reconstruction of leptons. Triggering on low transverse momentum (p_T) leptons, reconstructing leptons below a p_T of 50 GeV is key to enhancing the acceptance. This can be seen from the muon p_T distribution shown on Figure 2.2.

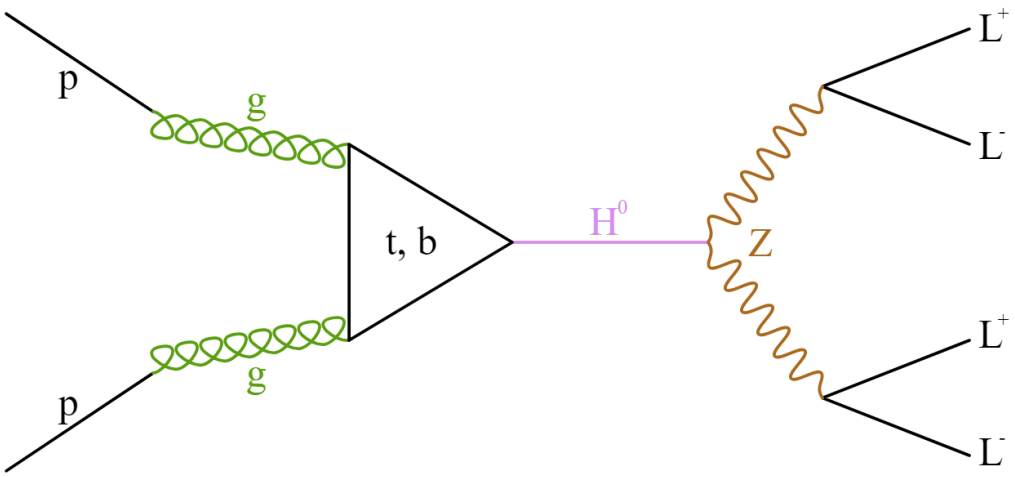

Figure 2.1: Feynman diagrams showing the "golden" channel associated with the low-mass (125 GeV) Higgs boson observed at the LHC. H$\longrightarrow ZZ^* \longrightarrow 4L$.

Using the existing L1 trigger algorithms and L1-menu information, it can be estimated that the minimum L1 acceptance rate would need to be 1500 kHz in order to maintain the same physics acceptance under 140 pile-up conditions [8]. If the environment rises to 200 pile-up, 4000 kHz bandwidth would be required, which exceeds the designed upgrade of the L1 trigger hardware. Adding tracking information to the L1 trigger system can reduce the rate substantially, to about 260 kHz for 140 pile-up and 500 kHz for 200 pile-up. Simulation results are shown in Figure 2.3. It is obvious that the algorithm with track information reduces the trigger rate.

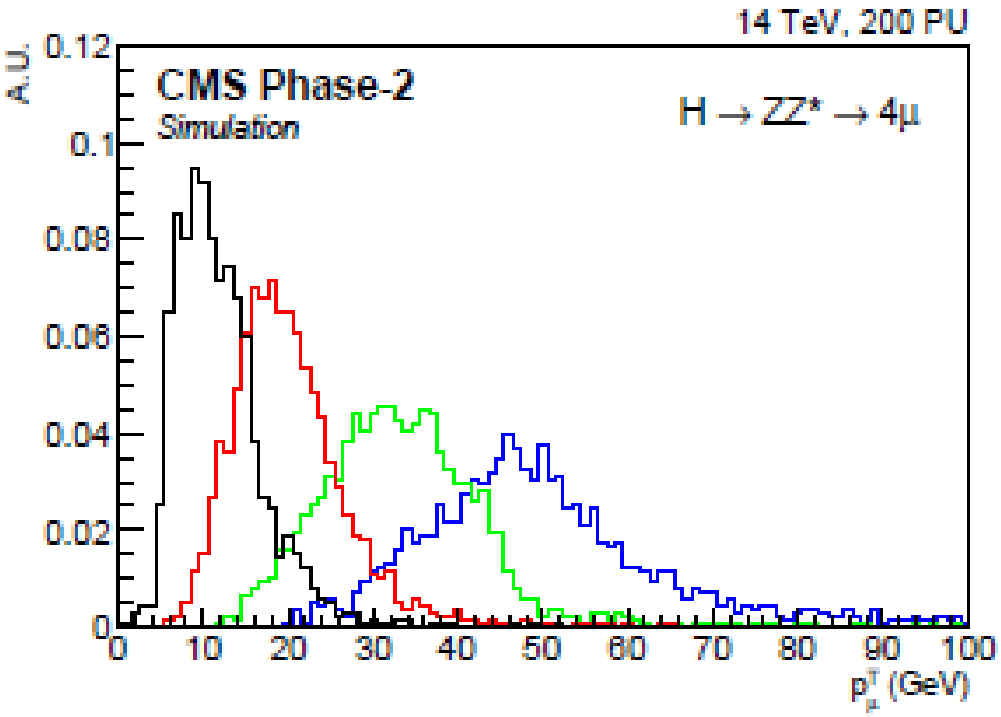

Figure 2.2: The distribution of p_T of the four muons in the Higgs decay "golden" channel. It is ordered from the smallest (black) to the largest (blue)

However, the estimated bandwidth above is still not enough. One reason is it should include a margin to cover uncertainties such as simulation imperfections and limitations in realising the L1 track based trigger in hardware, and the ability of other subsystems to provide the required L1 rate. The present estimates are also only representative of past operational experience. Studies are ongoing to estimate if key signals accessible only at the HL-LHC would benefit from larger acceptance rates. To cover these uncertainties, we specify a 50% larger rate for the overall L1 trigger, up to 750 kHz in 200 pile-up conditions, with enough margin for physics and experimental uncertainties.

The detector readout and HLT system will be upgraded, which will allow the L1 readout to increase from 100 kHz at present to 750 kHz, and the L1 latency to increase from 4 μsec to 12.5 μsec. The output rates of HLT will be up to 7.5 kHz (compared to 0.5 to 1 kHz at present). The L1 latency will be 12.5 μs which provides sufficient time for the L1 track trigger to do track reconstruction and matching with data from the muon system and calorimeter. L1 tracks need to be reconstructed

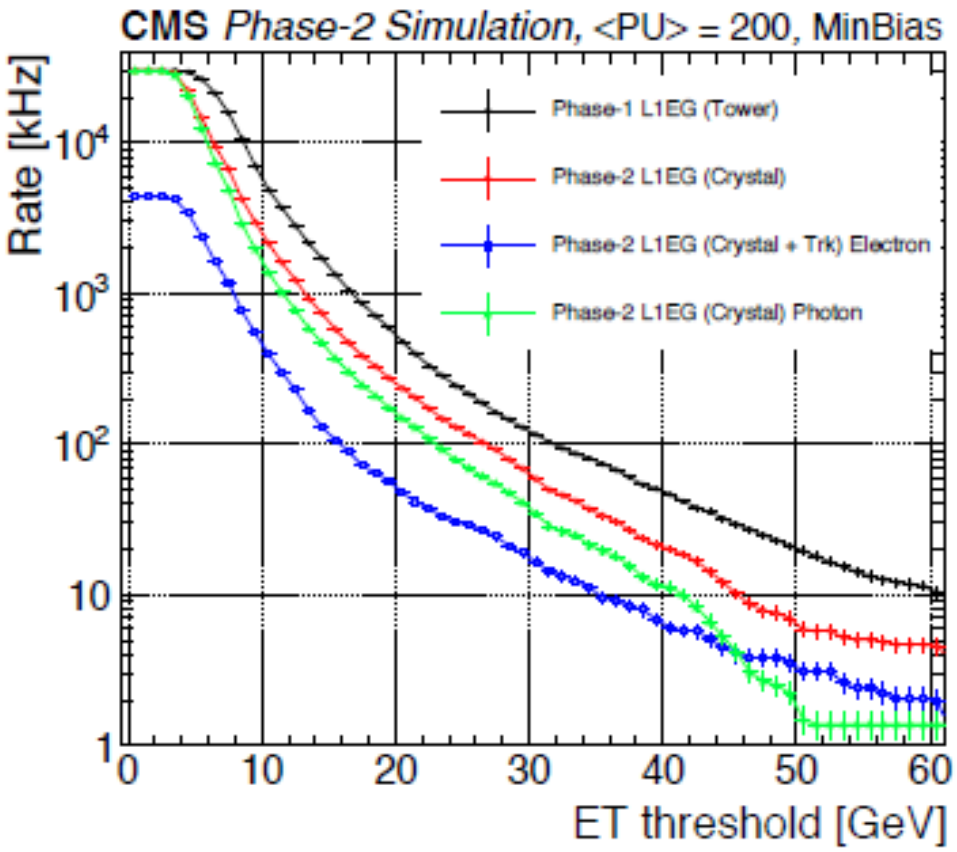

Figure 2.3: Expected rate for minimum-bias events using the single electron calorimeter trigger (for the barrel region only) as a function of trigger threshold. L1EG stands for the trigger to detect electrons and photon. Tower is defined as 5x5 crystals [19]

within 5 μs, including 1 μs to transmit data, in order to fit the overall L1 trigger latency.

2.2 The CMS tracker upgrade

The current tracker is designed to operate efficiently at a luminosity of 1×10^{34} cm^{-2}s^{-1}, an average pile-up of 20-30 collisions per bunch crossing, and an integrated luminosity up to 500 fb^{-1}. The detector will operate well until the level of radiation damage associated with data collection beyond 500 fb^{-1}. As the HL-LHC will increase the instantaneous luminosity by a factor more than five, there are several limitations in the present tracker system.

In the pixel sensors, radiation damage reduces the charge collection efficiency.

The charge sharing with neighbouring pixels decreases leading to the deterioration of spatial resolution, and the hit efficiency is reduced. Although the degradation can be compensated by increasing voltage and modifying the pixel cluster hit templates, eventually the reduced charge can not be mitigated [20]. In the strip tracker, irradiation increases the sensor depletion voltage and leakage current. The increase in leakage current can be compensated with low temperature by a cooling system, however, there is no way to mitigate the increased sensor depletion voltage. No double-sided strip modules can operate after 1000 fb^{-1} [21]. Thus the tracker system needs to be replaced completely during the upgrade in LS3.

The main requirements of the tracker upgrade are summarised as follows.

- *Radiation tolerance.* The upgraded tracker system needs to operate efficiently until the integrated luminosity reaches 3000 fb^{-1}, with an appropriate margin. A margin of the order of 50% is targeted, to accommodate both uncertainties in the FLUKA [22] simulations and the potential delivery of additional integrated luminosity, should the ultimate luminosity scenario be realized. For the Inner Tracker (based on silicon pixel modules, referred as IT), it is also required to be convenient to change modules and other elements that have suffered substantial radiation damage.

- *Increased granularity.* In HL-LHC, the benchmark of detector performance is 140-200 collisions per bunch crossing. In order to keep efficient tracking performance at such a high level of pile-up, a high channel density is required, keeping the channel occupancy around or below the per-cent level in the Outer Tracker (made from silicon modules with strip and macro-pixel sensors, referred as OT) and per mille level in the IT.

- *Improved two-track separation* The present track finding performance has a limitation in high energy jets, as the hits merge. In order to exploit a large amount of collision data in HL-LHC, two-track separation needs to be improved.

- *Reduced material in the tracking volume.* A lighter tracker system can benefit the performance, as particles interact with detector material, affecting the performance of both tracker and calorimeters.

- *Robust pattern recognition* In high pile-up conditions, it becomes increasingly difficult and time consuming to recognise track patterns. The upgrade of the tracker should enable efficient and fast track finding, especially at HLT.

- *Extended tracking acceptance* At present, the coverage of the tracker in the forward region is $|\eta| < 2.4$. An extended acceptance can benefit the CMS physics capability. The Phase-2 upgrade plans to expand efficient tracking coverage up to $|\eta| < 4$. For example, in the Higgs golden decay channel, extending tracking acceptance to $|\eta| = 3.0$ corresponds to a 15% increase in the acceptance for the four leptons with respect to the Run 2 detector [8].

- *Contribution to the Level-1 trigger* As discussed before, in the Phase-2 upgrade, tracking information from the tracker will be input to the L1 trigger decision system in order to improve the discriminating power of the event selection.

In the Phase-2 upgrade, a new tracker layout with six layers in the OT is planned, the minimum required to ensure robust track finding in the L1 trigger, shown in Figure 2.4.

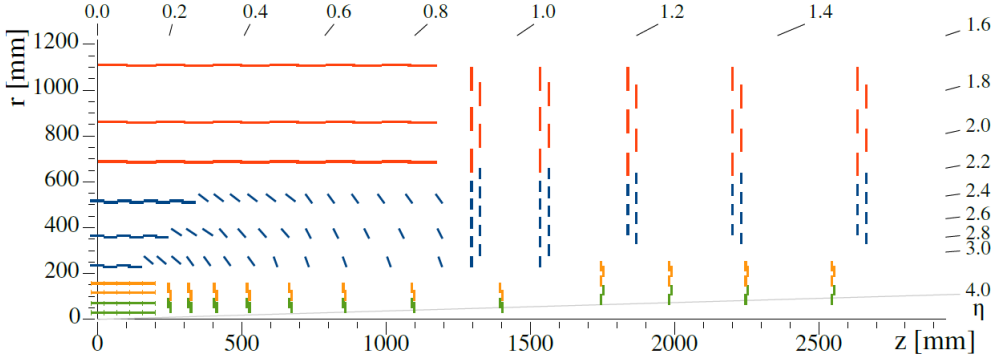

Figure 2.4: One quarter of Phase-2 tilted barrel tracker layout in η-z view. It includes six barrel layers, and five endcap disks. In the IT, the green lines refer to pixel modules with two readout chips, while the orange lines refer to pixel modules with four readout chips. In the OT, the red lines and blue lines represent two types of modules described below [8]

2.3 The Level-1 track trigger

In order to provide tracking information to the L1 trigger, the OT and module concept need upgrading. Local data reduction in the front-end electronics will allow data to be sent to the L1 trigger at 40 MHz.

Specifically, this can be achieved by the modules, known as "p_T modules", discarding signals from particles below a certain transverse momentum (p_T) threshold [23]. The moving charged particles are bent in the transverse plane by the 3.8 T magnetic field. The bending angle depends on the p_T of the particles. The modules are comprised of two single-sided closely-spaced sensors read out by a common front-end Application-Specific Integrated Circuit (ASIC) which correlates the signals in the two sensors and selects the hit pairs (referred to as "stubs") [8]. The p_T threshold depends on the acceptance window shown in Figure 2.5(a), which can be changed by programming the readout chip. There are different sensor spacings for the p_T modules, optimizing the p_T selection in the different parts of the tracker (Figure 2.5(b) and (c)).

There are two kinds of p_T modules: the PS modules consist of a strip and a macro-pixel sensor, and the 2S modules two strip sensors, shown in Figure 2.6. In PS modules, the strips are 2.4 cm in length while the strips in 2S modules have a

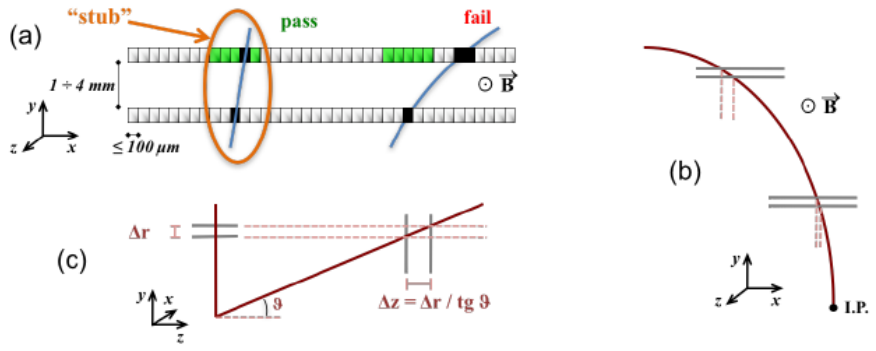

Figure 2.5: Sketch of p_T module concept. (a) Correlation of signals between two sensors rejects low-p_T particles.(b) For a given sensor spacing, two particles with the same p_T have a larger distance between two signals at large radius. (c) A larger sensor spacing in the endcap disk is needed in order to achieve the same p_T selection performance.

length of about 5 cm. The macro-pixel sensor is divided into macro-pixels with 1.5 mm length. Two kinds of modules measure z and r coordinates in the barrel and endcaps respectively. In the OT, the first three layers are PS modules in the radial region of 200-600 mm, shown in Figure 2.4 by blue. The 2S modules are in the outermost three layers from 600 mm in the radial region. In the endcaps, both PS and 2S modules are deployed in rings on disc-like structures. The PS modules are in the low radius area (lower than 700 mm) while the 2S modules equip the larger radius range.

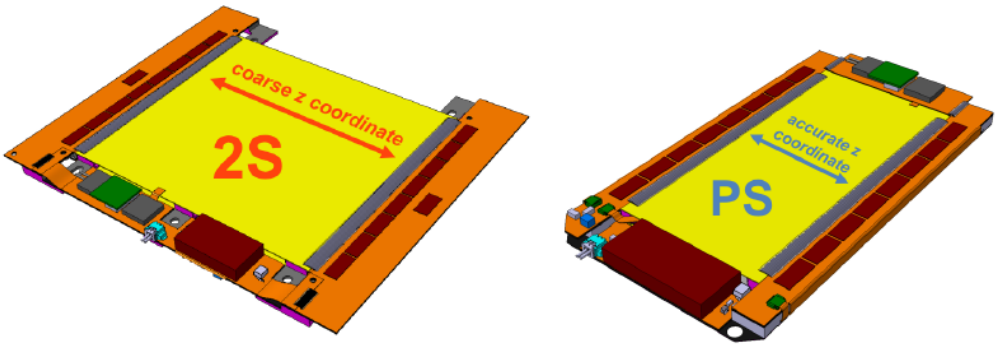

Figure 2.6: The 2S module is on the left and the PS module is on the right. The PS module has better z coordinate resolution

2.4 Hough transform

CMS has evaluated three different approaches for L1 tracking. One uses FPGAs and associative memory ASICs, and two of them are based on all-FPGA solutions with a Hough transform algorithm or road search algorithm. In this article, we focus on the all-FPGA solution using Hough transforms [8].

The Hough transform is a method for the recognition of complex patterns in pictures invented in 1962 [24], to detect tracks in bubble chambers. At present, the Hough transform is widely used in computer vision and image analysis. Here, it is used to recognise tracks from a set of stubs. The principle in general is to transform the stubs from points in ordinary space to a line in parameter space (Hough-space). If several different stubs are created by one track, the lines in parameter space will have a point of intersection. The first step is to transform stubs from the transverse plain to Hough-space. Then, a decision is made whether the stubs are created by one track.

In the transverse plane, charged particles are bent by the magnetic field. The curvature radius R (in cm) is a function of p_T (in GeV), magnetic field B (in Tesla) and charge q (in e):

$$R = \frac{P_T}{0.003qB} \tag{2.1}$$

Setting Φ as the angle of origin of the track in the transverse plane, while ϕ is the angle of the stub position and r is the distance of the stub to the origin, as shown in Figure 2.7, using the alternate segment theorem the relation between R, r, Φ and ϕ is:

$$\frac{r}{2R} = \sin(\phi - \Phi) \approx \phi - \Phi \tag{2.2}$$

It can be estimated that $\phi - \Phi$ is small for large transverse momentum particles (larger than 3 GeV), thus $\sin(\phi - \Phi) \approx \phi - \Phi$ is acceptable. Combining equation

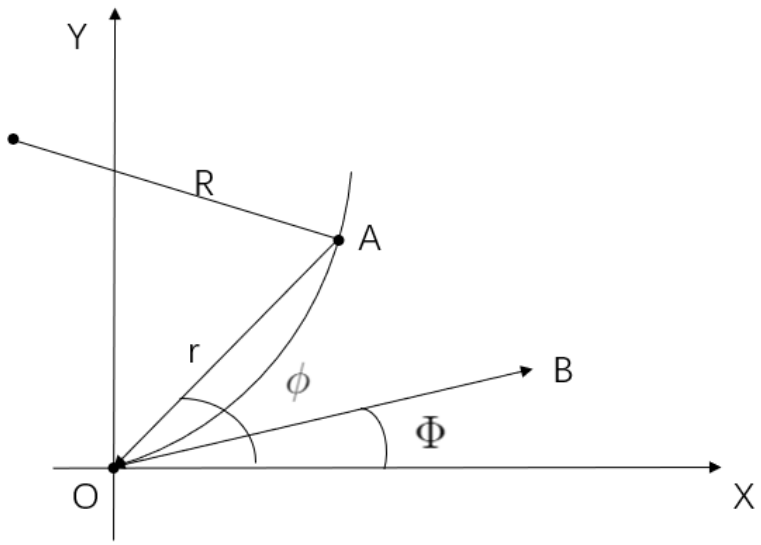

Figure 2.7: In transverse plane, the radial OB is a tangent at point O of arc OA, thus, $\angle BOx$ is Φ, $\angle AOx$ is ϕ

2.1 and equation 2.2 gives:

$$\Phi = \phi - \frac{0.0015qB}{p_T} \cdot r \tag{2.3}$$

This equation shows the transform from (r,ϕ) to the track parameter space (q/p_T,Φ), also known as Hough-space. An example is illustrated in Figure 2.8.

In Figure 2.8, since six lines in Hough-space intersect in a single point, we can conclude that the six stubs in the transverse plane are produced by one track. In this article, a track candidate is produced if at least five stubs from different tracker barrel layers or endcap disks accumulate at one point. In the region $0.89<|\eta|<1.16$, the requirement is reduced to four stubs from different layers, because there is a small gap between barrel and endcaps.

As shown in Figure 2.9. The L1 track finder is subdivided octant into 36 sub-sectors (16 in the transverse plain, 18 in the $r-z$ plain and octant contain 8 sub-sectors, thus $16 \times 18/8 = 36$), an independent Hough Transform is used in each sub-sector. In order to implement the Hough Transform, the Hough-space is separated into an array of cells. The horizontal axis is constrained by $|q/p_T| < q/p_T^{min}$, where $p_T^{min} = 3$ GeV. A compromise choice of array granularity is 32×64 cells in $q/p_T \times \Phi$,

which balances tracking performance and FPGA hardware resources.

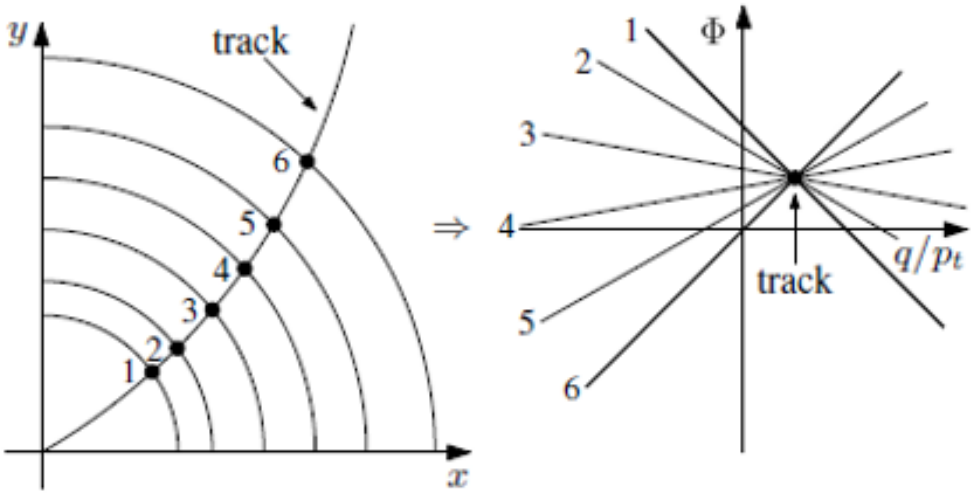

Figure 2.8: Example of a Hough Transform. The left sketch describes a track producing six stubs in six layers in one quarter of the transverse plane. The right sketch shows the six stubs in Hough-space, where the axes are the parameters (q/p_T,Φ). In Hough-space, each straight line represents a stub and the intersection of these lines represents a track [25]

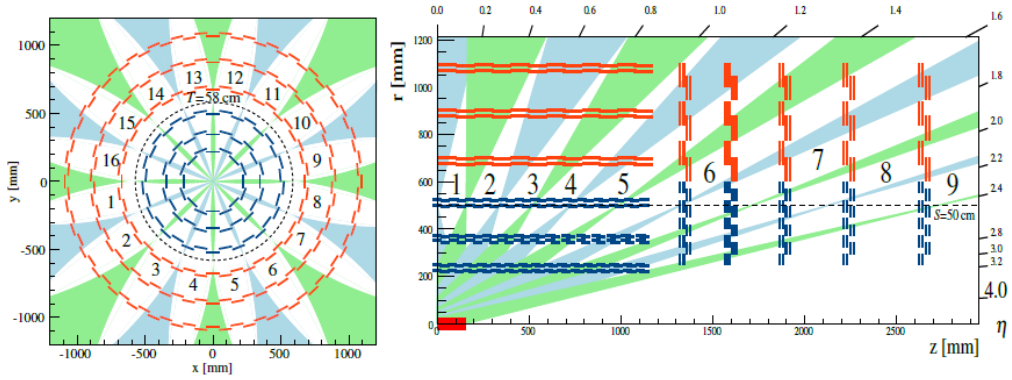

Figure 2.9: The segmentation of the tracker volume into ϕ sub-sectors on the left and η sub-sectors on the right. The white areas with numbers stand for the regions that are associated to only one sector, the blue and green regions are the overlap areas for neighbouring sectors where stubs may need to be assigned to both sectors.

Chapter 3

Performance of the Track Trigger

3.1 Analysis Method

The analysis described in this work is performed with a sample of simulated top quark pair production ($t\bar{t}$), with 8900 events at 14 TeV. The pile-up is 200 and the p_T cut is 3 GeV, with tilted tracker geometry. In the L1 track trigger, "track reconstruction" refers to the process of using information from hits on sensors and algorithm (e.g. Hough transform) to estimate the trajectory of charged particles (reconstruction tracks) and estimate their momentum and position. Simulated particles, referred to as tracking particles (TP) in CMSSW, are paired to reconstructed tracks for evaluating tracking efficiency, fake track rate, and other quantities [26].

If a reconstructed track has at least 75% of its hits originating from a single TP, this simulated particle (MatchTP) is associated with the reconstructed track. If a reconstructed track does not fit with any simulated particles, it is referred to as a fake track. The tracking efficiency (ϵ) is defined as the fraction of TPs associated to at least one reconstructed track, shown in equation 3.1. The efficiency depends not only on the algorithm, but also on the tracker properties, such as the material budget and the tracker layout.

$$\epsilon = \frac{N_m}{N_t} \tag{3.1}$$

N_t is the number of TPs, and N_m is the number of MatchTP. Both TP and MatchTP are required to have $p_T > 3$ GeV and $|\eta| < 2.4$.

3.2 Track trigger performance dependence on p_T

The track reconstruction efficiency as a function of p_T is shown in Figure 3.1, and Figure 3.2. It shows that the track reconstruction efficiency keeps high at about 95% from $p_T = 3$ GeV to $p_T = 100$ GeV. In Figure 3.1, as p_T increases, the effect of statistical fluctuations is observable, because the number of tracks reduces drastically at high p_T, shown in Figure 3.3. Figure 3.2 zooms in to the p_T range from 3 GeV to 10 GeV, which shows the efficiency has an increase at $p_T = 3$ GeV, from a bit lower than 90%, to a stable high efficiency performance around 95%. Although this is not as high as offline tracking efficiencies, a track trigger efficiency of 90-95% is more than adequate for most physics processes. For example, as shown in Figure 2.3, the thresholds for electron selection rises around 8 GeV in the low p_T range without the track trigger. Using the track trigger will keep the acceptance of the lower threshold (as shown in Figure 2.2) with only a 5-10% loss of efficiency. Figure 3.3 shows the number of TPs and MatchTPs as a function of p_T. It shows the number of MatchTPs is very close to the number of TPs in each bin, which means nearly all tracking particles are matched to corresponding reconstructed tracks.

The numbers of tracks and fake tracks are shown in Figure 3.4. Most of the fake tracks and tracks are in the low p_T range. As the p_T increases, the numbers of tracks and fake tracks decrease.

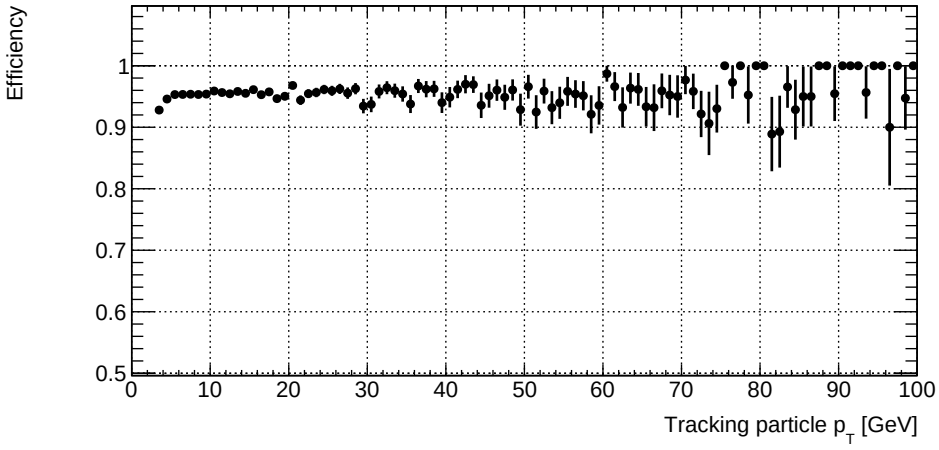

Figure 3.1: L1 track finding efficiency as a function of transverse momentum (p_T) for simulated $t\bar{t}$ events with 200 pile-up. Error bars represent binomial uncertainties.

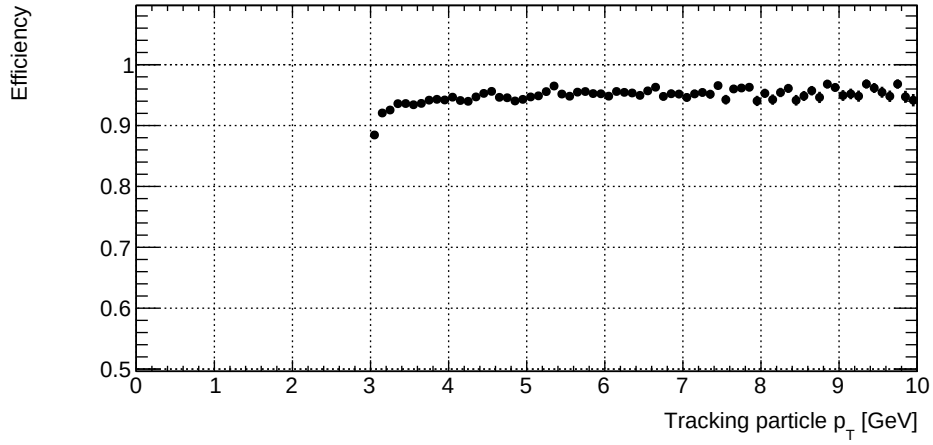

Figure 3.2: L1 track finding efficiency as a function of transverse momentum (p_T) for simulated $t\bar{t}$ events with 200 pile-up. Error bars represent statistical uncertainties.

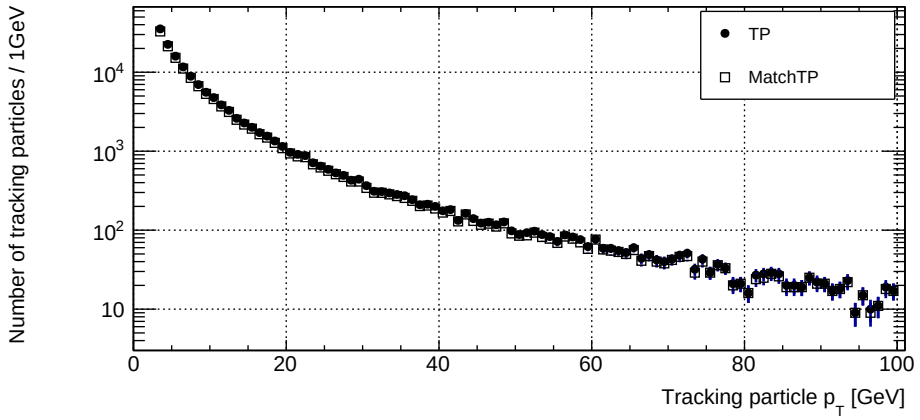

Figure 3.3: The number of TPs and MatchTPs as a function of transverse momentum (p_T) for simulated $t\bar{t}$ events with 200 pile-up. Error bars represent statistical uncertainties.

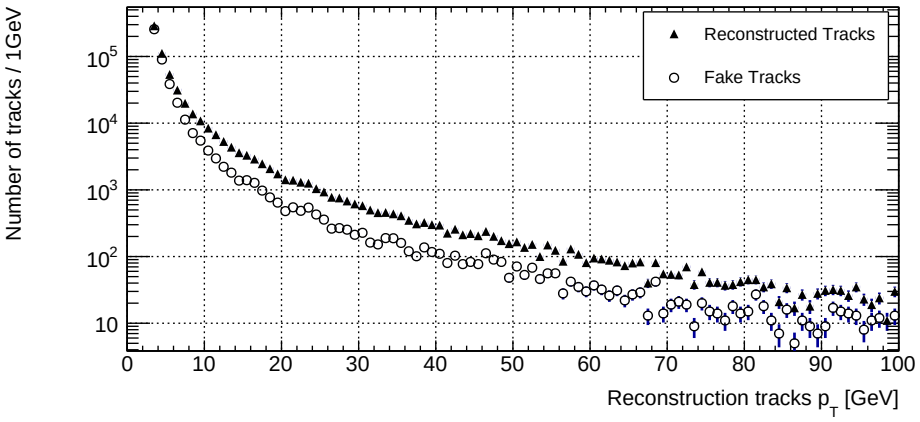

Figure 3.4: The number of tracks and fake tracks as a function of transverse momentum (p_T) for simulated $t\bar{t}$ events with 200 pile-up. Error bars represent statistical uncertainties.

3.3 Track trigger performance as function of angle

Figure 3.5 shows the overall efficiency as a function of η, ranging from -2.4 to 2.4. The efficiency is high at around 95% except at the end of the range (82%) with a 0.2 bin size. Some reconstructed tracks are out of range due to the η resolution, leading to the low edge efficiency. Figure 3.6 shows the numbers of TPs and MatchTPs in each bin (bin size is 0.1). The numbers of TPs and MatchTPs decrease with increasing $|\eta|$, and the MatchTPs follow the TPs closely, as expected from the high efficiency.

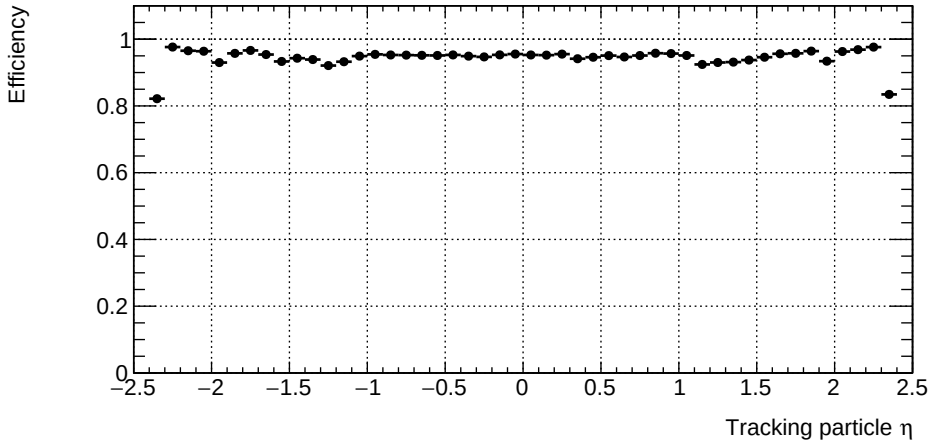

Figure 3.5: L1 track finding efficiency as a function of pseudorapidity (η) for simulated $t\bar{t}$ events with 200 pile-up. Error bars have been calculated using binomial errors, but are too small to be visible.

Figure 3.7 shows the number of reconstructed tracks and fake tracks. It shows two peaks around $|\eta| = 1.5$ for both tracks and fake tracks, although the number of particles generally decreases as $|\eta|$ increases. This can be understood from Figure 3.8. Taking the $\eta > 0$ range as an example, the number of reconstructed tracks rises from around $\eta \approx 0.9$ and reaches a peak at $\eta \approx 1.5$. After that, the number of reconstructed tracks decreases. In Figure 3.8, the black solid line represents a particle that will hit endcap modules and the dashed line stands for particles that will hit PS modules in the endcap. The η of the solid line is 0.9 while the η of the dashed line is 1.5, which helps to explain the result in Figure 3.7. There are three reasons for the rise from $\eta \approx 0.9$. The first reason is that a track candidate

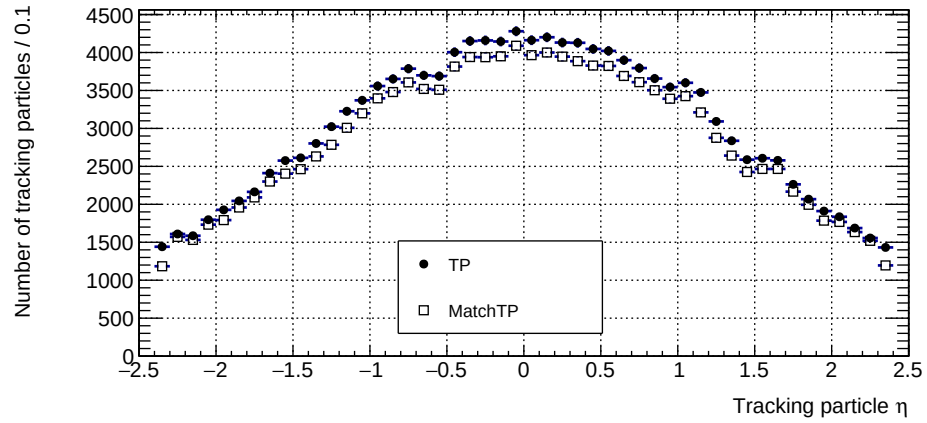

Figure 3.6: The number of TPs and MatchTPs as a function of pseudorapidity (η) for simulated $t\bar{t}$ events with 200 pile-up. The reason of unsmoothed points around $\eta = -0.5$ and $\eta = 1$ is statistical fluctuation.

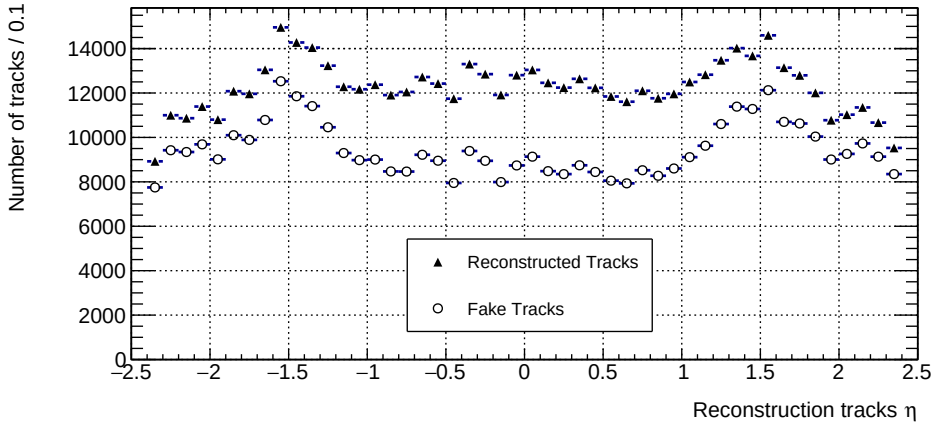

Figure 3.7: The number of tracks and fake tracks as a function of pseudorapidity (η) for simulated $t\bar{t}$ events with 200 pile-up.

is identified by less stubs (just four, five is normal) from $0.89 < |\eta| < 1.16$, which makes more tracks. The second reason is some particles pass through more than six layers, making more stubs, and more track candidates can be created. For example, the dashed line in Figure 3.8 passes through at least seven layers, which leads the numbers of tracks and fake tracks to reach the peak seen in Figure 3.7. The last reason is endcap 2S modules have larger uncertainty on the r coordinate than PS modules, creating fake tracks.

As a consequence, the particle hits more 2S modules in the endcap when η increases, leading to more fake tracks. If the η of a particle is larger than the dashed

line, it will hit PS modules in the endcap. As the PS module has better resolution in the r coordinate, and the number of particles decrease at large η range, shown in Figure 3.6, the number of tracks and fake tracks decreases as in Figure 3.7.

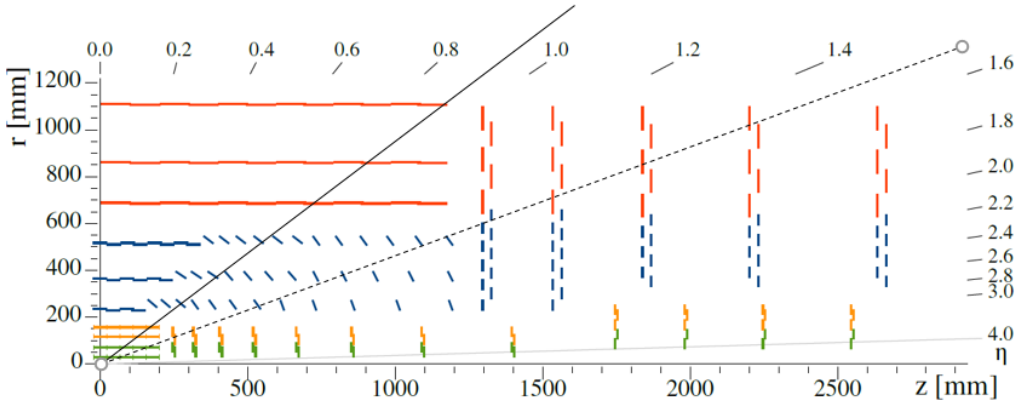

Figure 3.8: The symbol here is same as in Figure 2.4. The PS modules and 2S modules are represented by the red lines and blue lines respectively. The black solid line and black dashed line represent particle trajectories with $\eta = 0.9$ and $\eta = 1.5$ respectively.

3.3.1 Track trigger performance as function of angle for different z origins

The tracks from collisions do not emerge from one single point on the z axis, but are expected to come from primary vertices with a Gaussian distribution with $\sigma \approx 5cm$.

Efficiency is high when η is around 0 in all z regions, within statistical fluctuation, shown From Figure 3.9 to Figure 3.14. It is worth noting that there is a symmetry effect in the figures. Comparing Figure 3.9 and Figure 3.14, in Figure 3.9 there is a very low efficiency when $\eta < -2$ whereas Figure 3.14 has the corresponding effect when $\eta > 2$. It can be seen that the efficiency of reconstruction is low for the large η region which has same the sign as the z coordinate. Specifically, it can be seen from Figure 2.4 that tracks produced at $z > 0$, with large absolute values of η pointing to the right ($\eta > 2$) meet less layers, even through the geometry is tilted for the Phase-2 upgrade. The same effect happens for $z < 0$ such as in Figure 3.9 with large η.

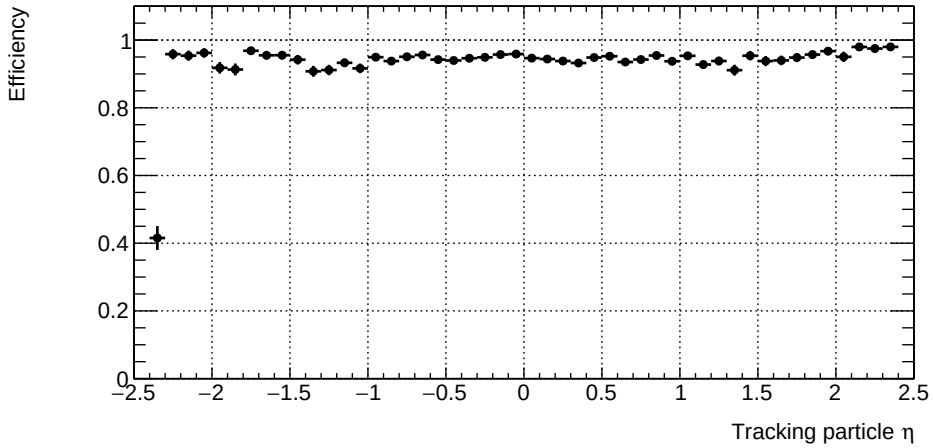

Figure 3.9: L1 track finding efficiency as a function of pseudorapidity η ($z < -5$ cm) for simulated $t\bar{t}$ events with 200 pile-up. Error bars represent binomial uncertainties.

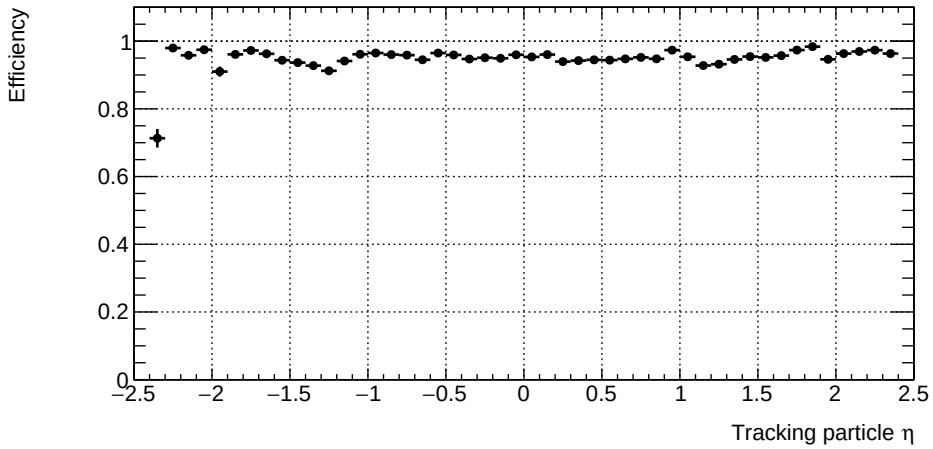

Figure 3.10: L1 track finding efficiency as a function of pseudorapidity η ($-5 < z < 2$ cm) for simulated $t\bar{t}$ events with 200 pile-up. Error bars represent binomial uncertainties.

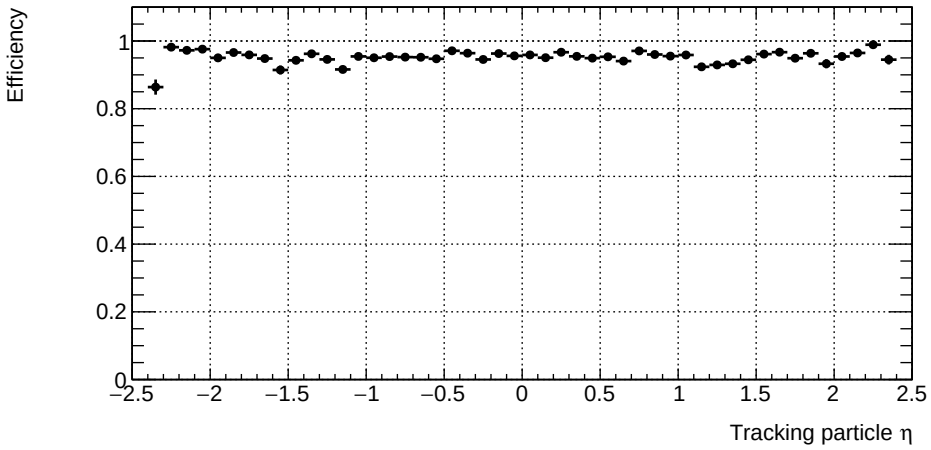

Figure 3.11: L1 track finding efficiency as a function of pseudorapidity η ($-2 < z < 0$ cm) for simulated $t\bar{t}$ events with 200 pile-up. Error bars represent binomial uncertainties.

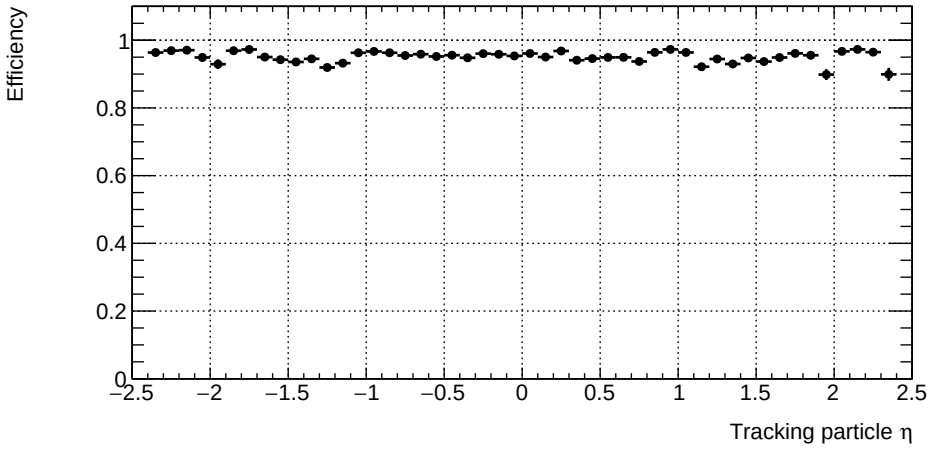

Figure 3.12: L1 track finding efficiency as a function of pseudorapidity η ($0 < z < 2$ cm) for simulated $t\bar{t}$ events with 200 pile-up. Error bars represent binomial uncertainties.

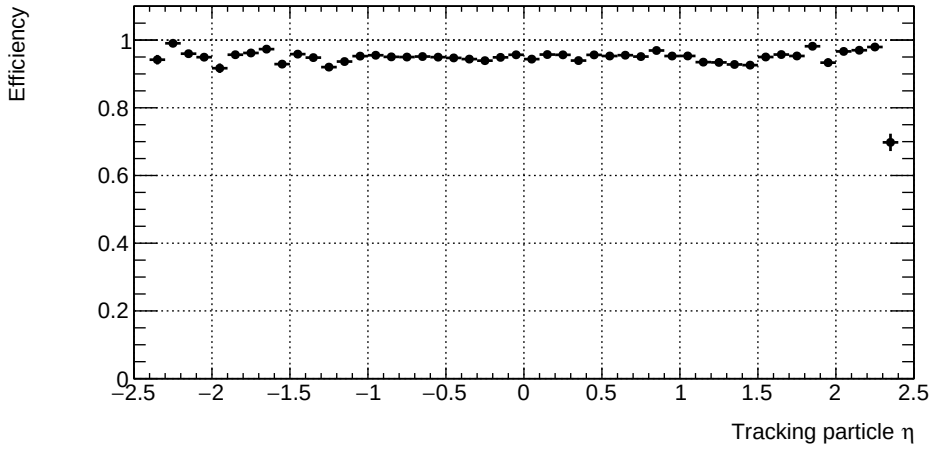

Figure 3.13: L1 track finding efficiency as a function of pseudorapidity η ($2 < z < 5$ cm) for simulated $t\bar{t}$ events with 200 pile-up. Error bars represent binomial uncertainties.

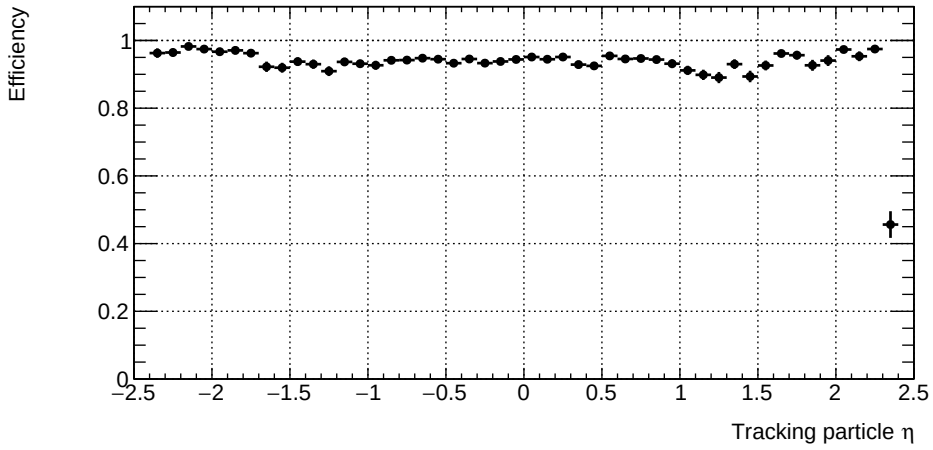

Figure 3.14: L1 track finding efficiency as a function of pseudorapidity η ($z > 5$cm) for simulated $t\bar{t}$ events with 200 pile-up. Error bars represent binomial uncertainties.

Chapter 4

Track Trigger Efficiency In Dense Tracking Environments

In order to quantify the reconstruction performance in a dense environment, we study the efficiency as a function of ΔR (distance to the closest jet axis), which is defined in Section 1.4.

Figure 4.1 shows the efficiency as a function of ΔR. The efficiency appears stable and high for small ΔR. It shows statistical fluctuations as ΔR increases, due to the decrease in the number of tracks. The distribution of the number of tracks can be seen in Figure 4.2. Over 95% of tracks are in the range $\Delta R < 0.4$.

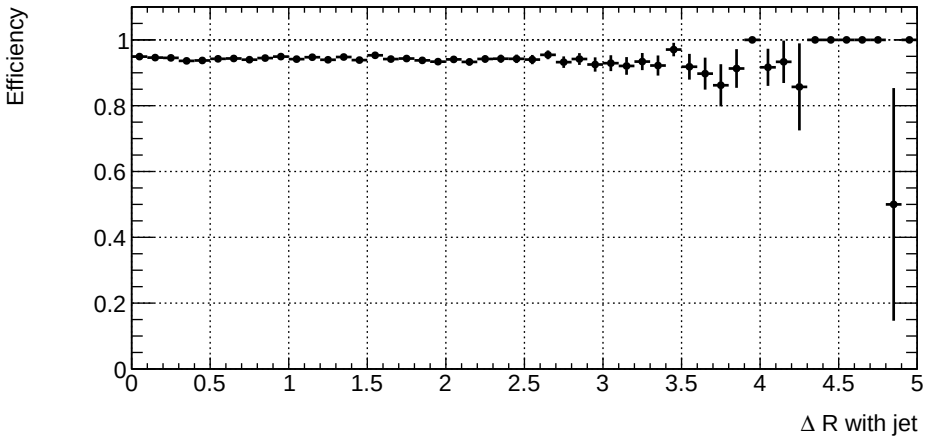

Figure 4.1: L1 track finding efficiency as a function of ΔR with the closest jet ($\Delta R < 5$) for simulated $t\bar{t}$ events with 200 pile-up. Error bars represent binomial uncertainties.

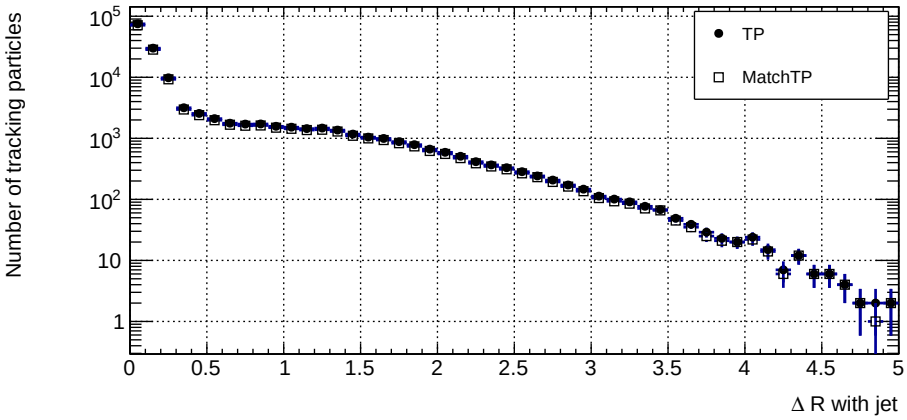

Figure 4.2: The number of TPs and MatchTPs as a function of ΔR with the closet jet ($\Delta R < 5$), for simulated $t\bar{t}$ events with 200 pile-up.

Figure 4.3 zooms into $\Delta R < 0.4$ in order to study the dense environment in jets. It can be seen that the efficiency keeps stable and high in the jet, reaching 94%. Figure 4.4 shows a peak at $\Delta R = 0.04$, which means the track distribution in jets is not random. The track density in jets is shown in Figure 4.6; the definition of density here is the number of tracks per unit area. It shows that the track density decreases as ΔR increases, which means the track density in jets reduces from the core to the edge.

Figure 4.5 shows the number of reconstructed tracks and fake tracks in jets. There is the same trend as seen with TPs in Figure 4.4 with a peak at $\Delta R = 0.04$, and the number of tracks is far more than the number of fake tracks in the low ΔR range. As ΔR increases, the difference between tracks and fake tracks shrinks rapidly. On the edge of jet, the number of tracks is far less than in the core of the jet.

Examining the reconstruction efficiency as a function of the angular distance (ΔR) between TPs, shows the track trigger performance in different density environments. Figure 4.7 shows a high efficiency around 93% for all values of ΔR. There is a small drop in efficiency at $\Delta R < 0.02$, because there are some tracks nearly overlaping with each other, which are hard to reconstruct with the current tracker granularity. Figure 4.8 shows the angular distance distribution between TPs

and MatchTPs. The shape of the plot means that most TPs and MatchTPs are separated an angular distance under $\Delta R = 0.1$.

It can be concluded that in $t\bar{t}$ events with a 200 pile-up environment, the track trigger system shows a good performance with 95% efficiency.

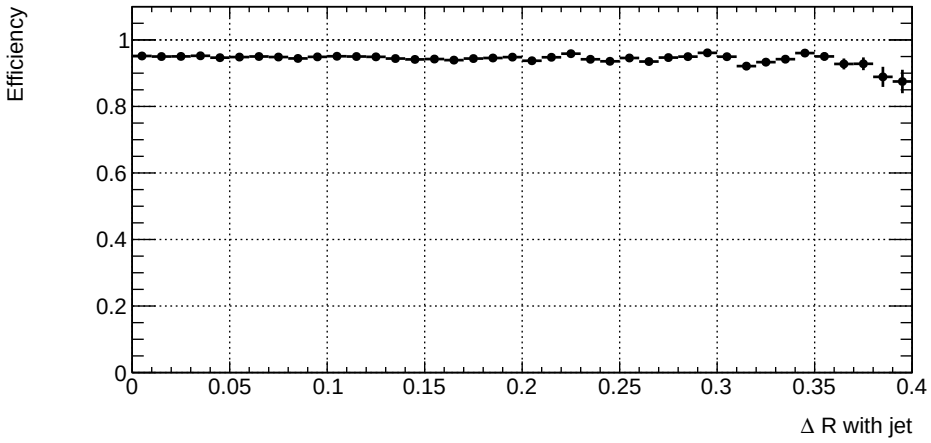

Figure 4.3: L1 track finding efficiency as a function of ΔR with jet ($\Delta R < 0.4$) for simulated $t\bar{t}$ events with 200 pile-up. Error bars represent binomial uncertainties.

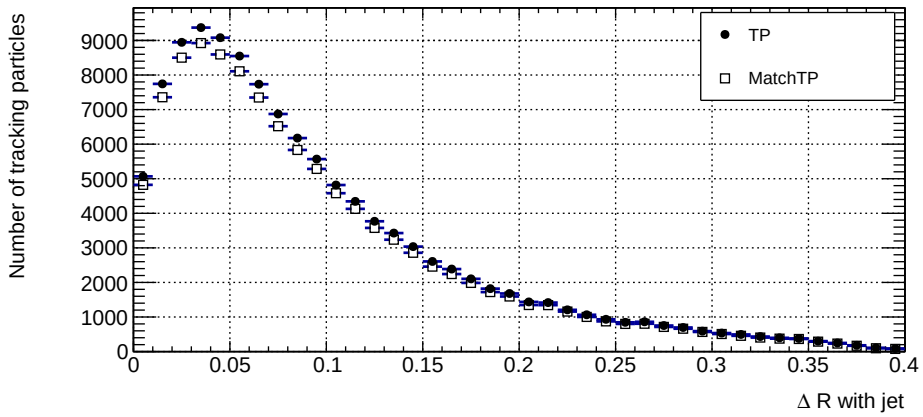

Figure 4.4: The number of TPs and MatchTPs as a function of ΔR with the closest jet ($\Delta R < 0.4$) for simulated $t\bar{t}$ events with 200 pile-up.

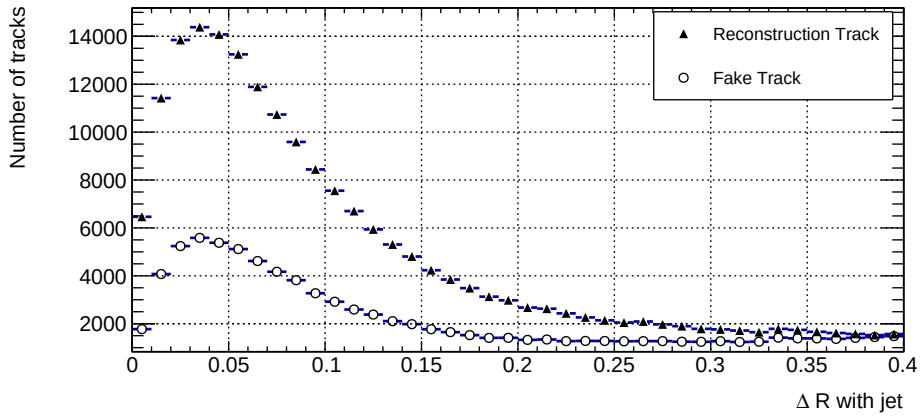

Figure 4.5: The number of tracks and fake tracks as a function of ΔR with the closest jet for simulated $t\bar{t}$ events with 200 pile-up.

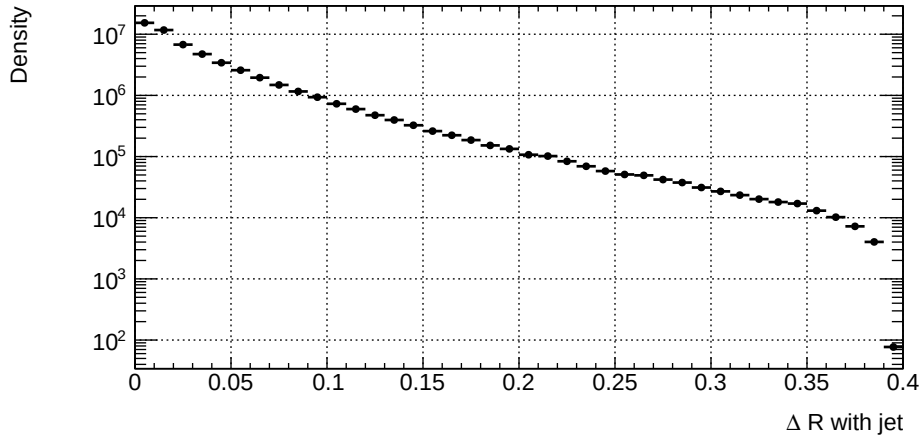

Figure 4.6: Tracks density in jet as a function of ΔR ($\Delta R < 0.4$) with the closest jet for simulated $t\bar{t}$ events with 200 pile-up.

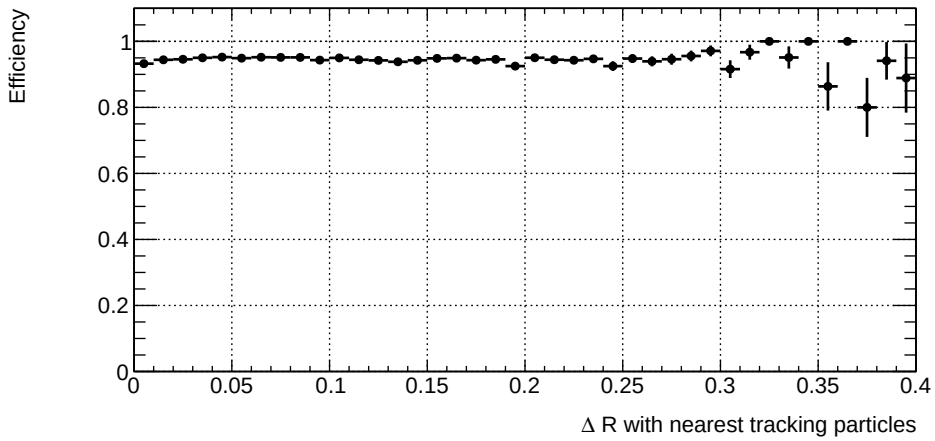

Figure 4.7: L1 track finding efficiency as a function of ΔR with the nearest TPs ($\Delta R < 0.4$) for simulated $t\bar{t}$ events with 200 pile-up. Error bars represent binomial uncertainties.

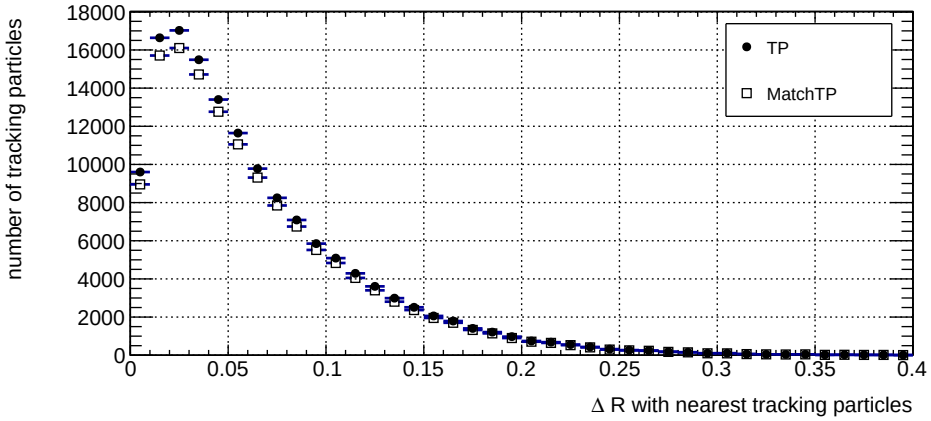

Figure 4.8: The number of TPs and MatchTPs as a function of ΔR with the nearest TPs ($\Delta R < 0.4$) for simulated $t\bar{t}$ events with 200 pile-up.

Chapter 5

Effect of the Cell Size in the Hough Transform

Here we compare three different cell sizes: 32x64 (32×64 cells in $q/p_T \times \Phi$ in the Hough space), 16x32 and 8x16, for the same data sample and pile-up condition. We change the number of bins in the Hough Transform in order to research the track trigger performance change.

Firstly, the plot of efficiency as a function of p_T is shown in Figure 5.1. The 32x64 cell size has an obviously higher efficiency than the others, especially in the range of $p_T < 50$ GeV, reaching around 95%. The 16x32 cell size follows the 32x64 cell size closely while the 8x16 cell size shows a comparatively low performance of around 87%. When the p_T is larger than 50 GeV, the plots are consistent within statistical uncertainties.

Figure 5.2 shows the efficiency as a function of η. The efficiency is stable and high over the whole range except for the end points, where it is lower than 85%. The plot also shows the larger cell size has lower efficiency.

The plot of efficiency with ΔR (with respect to the center of the nearest jet) is shown in Figure 5.3. It can be seen from Figure 5.3 in the range $\Delta R > 0.15$ there is no difference between the three cell sizes. However in the low ΔR range, there is an obvious difference. The larger cell size gives lower performance, reaching just lower

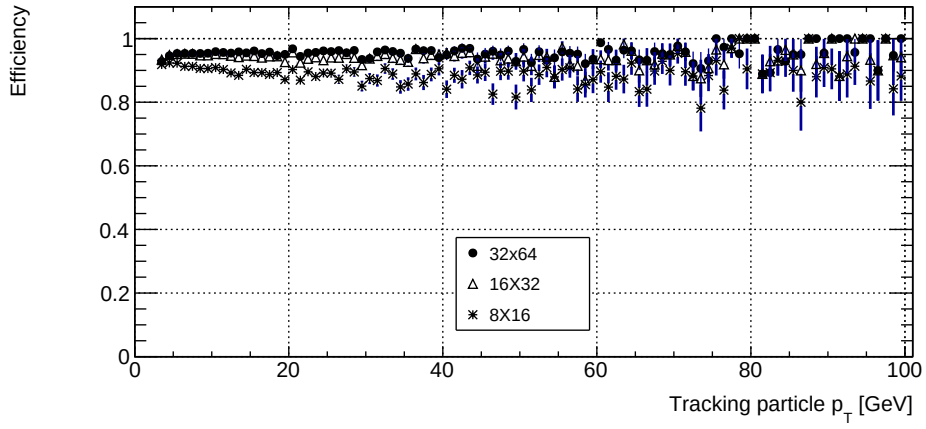

Figure 5.1: L1 track finding efficiency as a function of transverse momentum (p_T) for simulated $t\bar{t}$ events with 200 pile-up with different cell sizes. Error bars represent binomial uncertainties.

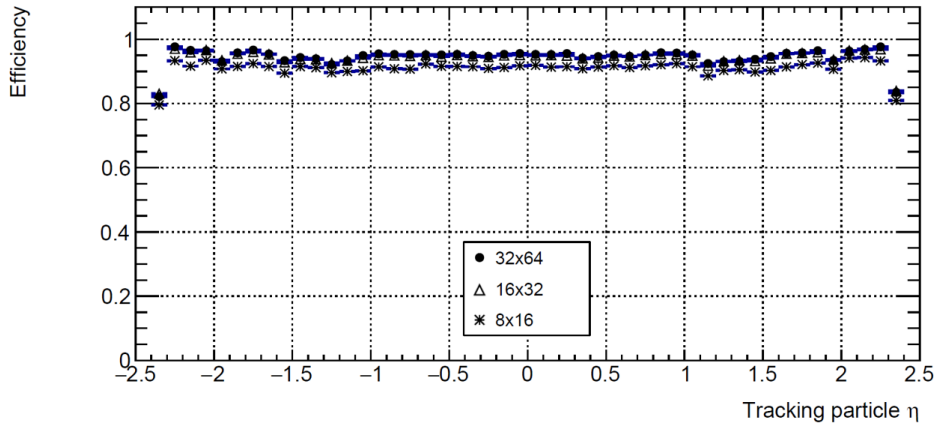

Figure 5.2: L1 track finding efficiency as a function of pseudorapidity (η) for simulated $t\bar{t}$ events with 200 pile-up different cell sizes. Error bars have been calculated using binomial errors, but are too small to be visible.

than 85% at around $\Delta R = 0.02$. The 32x64 and 16x32 cells show a high efficiency of around 95%. Figure 5.4 shows the number of MatchTPs (with different cell sizes) as a function of ΔR, ranging from 0 to 0.4. All MatchTPs have the same trend, increasing from $\Delta R = 0$ and reaching a peak at around $\Delta R = 0.04$. It can be seen for a larger cell size such as 8x16, the number of MatchTPs is lower, which indicates the efficiency is lower.

Figure 5.5 shows the number of fake tracks as a function of ΔR from 0 to 0.4. As we use the same data sample and pile-up conditions, we can compare the relative performance. All curves show a similar trend. They start with an increase, reach

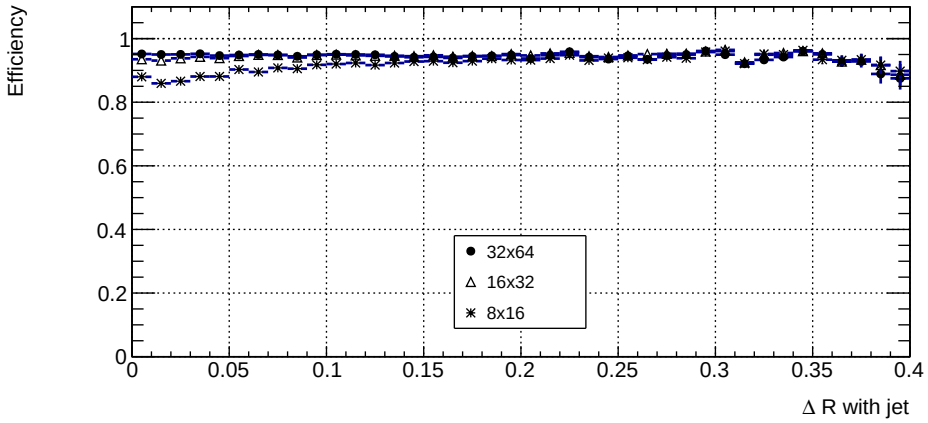

Figure 5.3: L1 track finding efficiency as a function of ΔR with jet ($\Delta R < 0.4$) for simulated $t\bar{t}$ events 200 pile-up different cell size. Error bars represent binomial uncertainties.

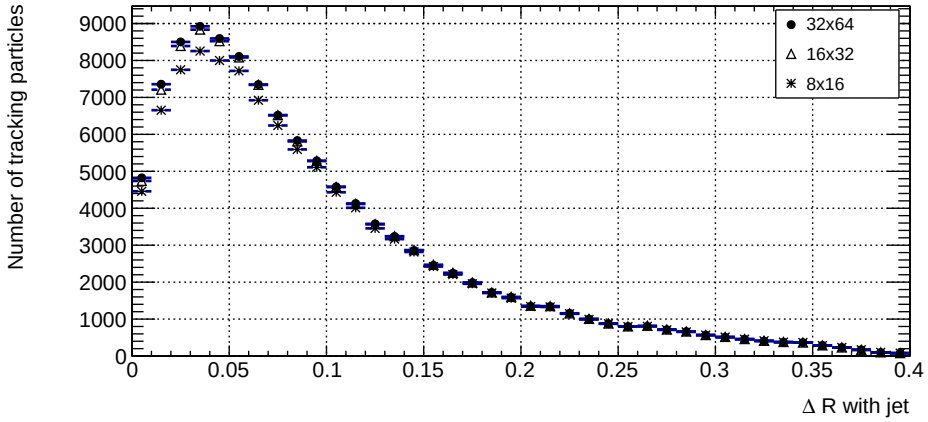

Figure 5.4: The number of MatchTPs as a function of ΔR with the closest jet ($\Delta R < 0.4$) for simulated $t\bar{t}$ events 200 pile-up different cell sizes.

a peak around $\Delta R = 0.03$, then decreases. Different relationships in different ΔR regions can be observed. Specifically, in the low ΔR range (from 0 to 0.06), for the larger cell size, the number of fake tracks is small. When $\Delta R > 0.11$, the larger cell size has more fake tracks.

The explanation of this phenomenon is shown in Figure 5.6. In the center of a jet (low ΔR range), the tracks are dense and stubs are close to each other, which leads to the fake tracks in the Hough-space being close, as shown on the left sketch in Figure 5.6. If the cell size is large like the bold square, the algorithm recognises two fake intersections as one fake track. If the cell size is small, such as the four

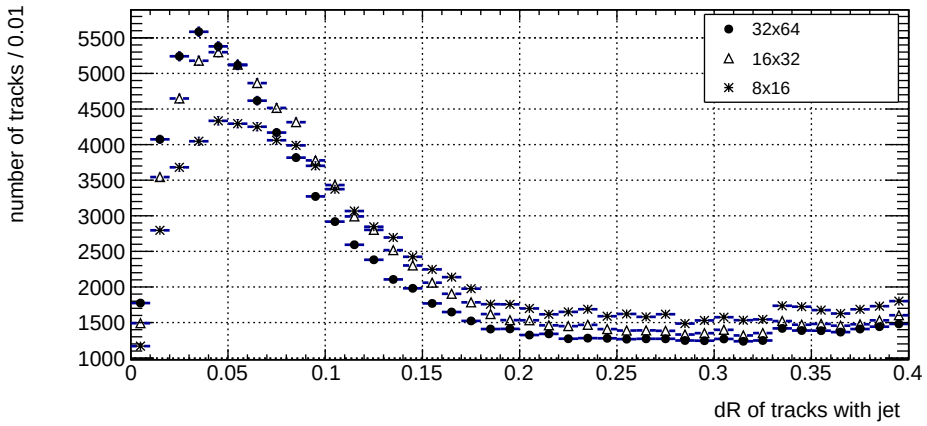

Figure 5.5: The number of fake tracks as a function of ΔR with the closest jet ($\Delta R < 0.4$) for simulated $t\bar{t}$ events with 200 pile-up in different cell size.

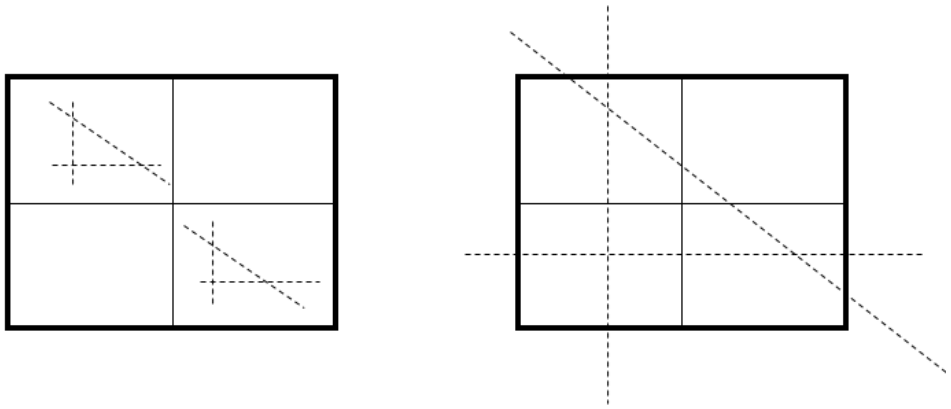

Figure 5.6: A sketch in Hough-space, triangle stands for fake tracks. The bold square stands for large cell size and four small squares means small cell size.

small squares, the algorithm regards two fake intersections as two fake tracks. On the outskirts of a jet (large ΔR range), the tracks are not as dense as in the core of the jet, so the larger cell size has more fake tracks, shown in the right sketch in Figure 5.6, it can be seen that the algorithm using a larger cell size (bold square) produces a fake track, while the algorithm using a small cell size (a quarter of large cell size) will not produce a fake track.

It can be concluded that in $t\bar{t}$ events with a 200 pile-up environment, the track trigger system with 32x64 cell size shows a higher performance than larger cell size.

Chapter 6

Conclusion

The HL-LHC will challenge the CMS detector and trigger system. One of the most important upgrades will be the addition of track information to the Level-1 trigger system. The CMS track trigger is important to keep physical sensitivity in HL-LHC data taking.

The performance of the proposed CMS track trigger system shows high and stable results for different p_T and η. The layout of the tracker has an influence on the number of reconstructed tracks. For tracks originating from $z \neq 0$, the track trigger performance is high except for at large $|\eta|$. The reason for the low efficiency at large $|\eta|$ is the tracker layout. The tracks originating from $z > 0$ ($z < 0$) meet less layers on the direction of $z > 0$ ($z < o$) at large $|\eta|$. In dense tracking environments, the track trigger system shows a high performance. We also present the track density and track distribution in jets in order to prove the high performance in dense environments. In this article, a Hough transform is used to recognise tracks. By changing the cell size of the Hough transform, the performance of the track trigger system changes. The best performance is obtained with 32x64 cells in each sector. The Hough transform has a different performance between dense and sparse track environments. A smaller cell size produces more fake tracks in a dense environment while a larger cell size produces more fake tracks in a loose environment.

In this article, the track trigger system shows a good performance in different

conditions. It can be expected that the track trigger system will meet the challenges of the HL-LHC.

Bibliography

[1] David Griffiths. *Introduction to elementary particles*. John Wiley & Sons, 2008.

[2] G Bernardi, M Carena, and T Junk. Higgs bosons: theory and searches. *Reviews of Particle Data Group: Hypothetical particles and Concepts*, pages 10–11, 2007.

[3] Dave Fehling. The standard model of particle physics: A lunchbox's guide. *The Johns Hopkins University, Retrieved on*, pages 12–03, 2008.

[4] Lisa Randall and Raman Sundrum. Large mass hierarchy from a small extra dimension. *Physical Review Letters*, 83(17):3370, 1999.

[5] Gerard Jungman, Marc Kamionkowski, and Kim Griest. Supersymmetric dark matter. *Physics Reports*, 267(5-6):195–373, 1996.

[6] Lyndon Evans and Philip Bryant. Lhc machine. *Journal of instrumentation*, 3(08):S08001, 2008.

[7] W. Herr, B. J. Holzer, and B. Muratori. *6.4 Concept of Luminosity*, pages 140–146. Springer Berlin Heidelberg, Berlin, Heidelberg, 2013.

[8] CMS collaboration et al. The phase-2 upgrade of the cms tracker technical design report. Technical report, CERN-LHCC-2017-009, CMS-TDR-17-001, 2017.

[9] Serguei Chatrchyan, Vardan Khachatryan, Albert M Sirunyan, Armen Tumasyan, Wolfgang Adam, Ernest Aguilo, T Bergauer, M Dragicevic, J Erö, C Fabjan, et al. Observation of a new boson at a mass of 125 gev with the cms experiment at the lhc. *Physics Letters B*, 716(1):30–61, 2012.

[10] Atlas Collaboration et al. Observation of a new particle in the search for the standard model higgs boson with the atlas detector at the lhc. *arXiv preprint arXiv:1207.7214*, 2012.

[11] CMS collaboration, LHCb Collaboration, et al. Observation of the rare bs0→ μ+ μ- decay from the combined analysis of cms and lhcb data. *Nature*, 522(7554):68–72, 2015.

[12] Giorgio Apollinari, O Brüning, T Nakamoto, and Lucio Rossi. High luminosity large hadron collider hl-lhc. *arXiv preprint arXiv:1705.08830*, 2017.

[13] Georges Aad, Brad Abbott, Jalal Abdallah, S Abdel Khalek, O Abdinov, Rosemarie Aben, Babak Abi, Maris Abolins, OS AbouZeid, Halina Abramowicz, et al. Search for higgs boson pair production in the γ γ b b^{-} final state using p p collision data at s= 8 tev from the atlas detector. *Physical review letters*, 114(8):081802, 2015.

[14] CMS collaboration et al. Technical proposal for the phase-ii upgrade of the cms detector. *CERN, CERN-LHCC-2015-010. LHCC-P-008*, 2015.

[15] CMS collaboration et al. The phase-2 upgrade of the cms l1 trigger interim technical design report. *CERN, Geneva, Tech. Rep. CERN-LHCC-2017-013. CMS-TDR-017, Sep*, 2017.

[16] CMS collaboration et al. The cms trigger system. *arXiv preprint arXiv:1609.02366*, 2016.

[17] R Brandelik, W Braunschweig, K Gather, V Kadansky, K Lübelsmeyer, P Mättig, H-U Martyn, G Peise, J Rimkus, HG Sander, et al. Evidence for planar events in e+ e- annihilation at high energies. *Physics Letters B*, 86(2):243–249, 1979.

[18] CMS Collaboration et al. Cmssw application framework. *URL: https://twiki. cern. ch/twiki/bin/view/CMSPublic/Work BookCMSSWFramework*, 2006.

[19] CMS Collaboration. The Phase-2 Upgrade of the CMS L1 Trigger Interim Technical Design Report. Technical Report CERN-LHCC-2017-013. CMS-TDR-017, CERN, Geneva, Sep 2017. This is the CMS Interim TDR devoted to the upgrade of the CMS L1 trigger in view of the HL-LHC running, as approved by the LHCC.

[20] A Dominguez, D Abbaneo, K Arndt, N Bacchetta, A Ball, E Bartz, W Bertl, G M Bilei, G Bolla, H W K Cheung, M Chertok, S Costa, N Demaria, Daniel Dominguez Vazquez, K Ecklund, W Erdmann, K Gill, G Hall, K Harder, F Hartmann, R Horisberger, W Johns, H C Kaestli, K Klein, D Kotlinski, S Kwan, M Pesaresi, H Postema, T Rohe, C Schäfer, A Starodumov, S Streuli, A Tricomi, P Tropea, J Troska, F Vasey, and W Zeuner. CMS Technical Design Report for the Pixel Detector Upgrade. Technical Report CERN-LHCC-2012-016. CMS-TDR-11, Sep 2012. Additional contacts: Jeffrey Spalding, Fermilab, Jeffrey.Spalding@cern.ch Didier Contardo, Universite Claude Bernard-Lyon I, didier.claude.contardo@cern.ch.

[21] Markus Friedl. *The CMS silicon strip tracker and its electronic readout.* PhD thesis, Vienna, Tech. U., 2001.

[22] A Ferrari, Paola R Sala, A Fassò, and Johannes Ranft. *FLUKA: A multi-particle transport code (program version 2005).* CERN Yellow Reports: Monographs. CERN, Geneva, 2005.

[23] Costas Foudas, A Rose, J Jones, and G Hall. A study for a tracking trigger at first level for cms at slhc. *arXiv preprint physics/0510227*, 2005.

[24] P.V.C. Hough. Method and means for recognizing complex patterns (us.patent). 12 1962.

[25] Christian Amstutz, FA Ball, MN Balzer, J Brooke, L Calligaris, D Cieri, EJ Clement, G Hall, TR Harbaum, K Harder, et al. An fpga-based track

finder for the l1 trigger of the cms experiment at the high luminosity lhc. In *Real Time Conference (RT), 2016 IEEE-NPSS*, pages 1–9. IEEE, 2016.

[26] CMS collaboration et al. Description and performance of track and primary-vertex reconstruction with the cms tracker. *Journal of Instrumentation*, 9(10):P10009, 2014.